

UNIVERSITY OF OKLAHOMA

GRADUATE COLLEGE

MECHANICAL CHARACTERIZATION OF POLYDIMETHYLSILOXANE

A THESIS

SUBMITTED TO THE GRADUATE FACULTY

in partial fulfillment of the requirements for the

Degree of

MASTER OF SCIENCE

By

MARK OLIMA
Norman, Oklahoma
2017

MECHANICAL CHARACTERIZATION OF POLYDIMETHYLSILOXANE

A THESIS APPROVED FOR THE
SCHOOL OF AEROSPACE AND MECHANICAL ENGINEERING

BY

Dr. Mrinal Saha, Chair

Dr. Yingtao Liu, Co-Chair

Dr. M. Cengiz Altan

ACKNOWLEDGMENTS

Firstly, I would like to express my gratitude to Prof. Mrinal Saha of School of Aerospace & Mechanical Engineering at The University of Oklahoma at Norman, Oklahoma for providing me the great opportunity to be involved in this project as a member of his research group and all the support he has given to me during my graduate life. This project would not be done without his guidance and help. I would also like to thank Prof. Yingtao Liu, his immense knowledge and creative ideas were key motivations throughout this project and his encouragement inspired my enthusiasm to work hard for the success of my graduate life. Lastly, I would also like to thank Prof. M. Cengiz Altan for his encouragement from my early days as an undergraduate student.

Foremost, I would like to thank my family for the support from my first day of school. Their understanding and encouragement created a unique environment for my education in the United States of America, from Nairobi, Kenya. I also want to thank Mr. David Riley and Mrs. Ann Riley for all their kindness and helps given to me in my graduate life. Last but not least, I want to thank my best friends, Robyn Birch, Kevin Ndege, Shoieb Chowdhury, Jessica Mwaura and Wenyan Luo. Their supports substantially lessened my burden of writing this dissertation.

TABLE OF CONTENTS

ACKNOWLEDGMENTS	iv
LIST OF FIGURES	vii
LIST OF TABLES.....	x
ABSTRACT	xi
CHAPTER 1: INTRODUCTION.....	1
1.1 Polydimethylsiloxane	3
1.2 Strain measurement.....	6
1.3 Digital Image Correlation.....	8
1.4 Outline	9
CHAPTER 2: THEORY OF DIC.....	10
2.1 Introduction	10
2.2 Methodology.....	10
CHAPTER 3: EXPERIMENTAL METHOD.....	16
3.1 Material Preparation.....	16
3.2 Material Characterization	20
3.2.1 Density	20
3.2.2 Dynamic Mechanical Analysis	23
3.2.3 Thermogravimetric Analysis	28
3.3 Mechanical Testing.....	29
CHAPTER 4: RESULTS AND DISCUSSION	32
4.1 Dynamic Mechanical Analysis	32
4.2 Thermogravimetric Analysis	37
4.3 Finite Element Analysis	41
4.4 Mechanical Characteristic Analysis of PDMS in Tension.....	45

4.5 Mechanical Characteristic of PDMS in Compression	56
4.6 Mechanical Property Characterization of PDMS in Tension	62
4.7 Mechanical Property Characterization of PDMS in Compression	66
4.8 Effect of cure temperature on Sylgard® 184.....	68
4.9 Effect of silica content on Gelest.....	70
CHAPTER 5: SUMMARY AND FUTURE WORK.....	72
REFERENCES	74
APPENDIX.....	78
Correlation algorithm : cporr_mod.m.....	78

LIST OF FIGURES

Figure 1. Nonlinear hyper-elastic models of PDMS [4].	2
Figure 2. Chemical Structure of PDMS [8].	5
Figure 3. 3D structure of a PDMS molecule [14].	5
Figure 4. Schematic of digital image correlation methodology [29].	10
Figure 5. Subset before and after deformation [29].	11
Figure 6. PDMS Sylgard® 184 Kit with Part A and Part B [32].	16
Figure 7. (a) Compression sample mold (b) Tension sheet mold.	18
Figure 8. (a) ASTM D412-C Tension die (b) ASTM D412-C dimensions.	19
Figure 9. (a) Video Extensometer Tension Sample (b) DIC Tension Sample (c) DIC Compression Sample.	19
Figure 10. AccuPyc II micrometrics™.	20
Figure 11. Effect of cure temperature on density of Sylgard™ sample.	22
Figure 12. Effect of silica on density of Gelest™ samples.	23
Figure 13. The relationship of the applied sinusoidal stress to strain is shown, with the resultant phase lag and deformation [36].	25
Figure 14. Modulus values change with temperature and transitions in materials [36].	27
Figure 15. Sylgard® sample in tension ready for DMA test.	28
Figure 16. TA Q100 Thermogravimetric Analysis Instrument.	29
Figure 17. (a) PDMS sample setup in tension (b) Instron Single Colum Machine (c) Canon® EOS Rebel T5 Camera[38].	30
Figure 18. Video extensometer setup.	31
Figure 19. Storage modulus and tan delta as a function of temperature of Sylgard sample cured at 25°C.	32
Figure 20. Published storage modulus and tan delta as a function of temperature for Sylgard 184 [40].	33
Figure 21. Storage modulus as a function of temperature for Sylgard samples cured at different temperatures.	34
Figure 22. Storage modulus, loss modulus and tan delta as a function of temperature for Sylgard cured at 25°C.	35

Figure 23. Storage modulus, loss modulus and tan delta as a function of temperature for Sylgard [41].	35
Figure 24. Loss modulus as a function of temperature of Sylgard samples cured at different temperatures.	35
Figure 25. Tan delta for Sylgard samples cured at different temperatures.	36
Figure 26. Weight loss as a function of temperature for Gelest samples.	38
Figure 27. Differential weight change as a function of temperature for Gelest samples.	38
Figure 28. Residual mass as a function of silica content after TGA test for all Gelest samples.	40
Figure 29. Weight loss as a function of temperature for Sylgard samples.	40
Figure 30. Differential weight change as a function of temperature for Sylgard samples.	41
Figure 31. Finite Element Analysis at 10% strain showing uniform strain on the gage section.	42
Figure 32. Finite Element Analysis at 10% strain showing uniform stress on the gage section.	42
Figure 33. Cross-section of Finite Element Analysis at 10%.	43
Figure 34. Strain as a function of position from cross-section FEA.	43
Figure 35. Stress as a function of position from cross-section FEA.	44
Figure 36. Stress-strain relationship of different strain measurement techniques.	45
Figure 37. Exposed strain regions of PDMS sample.	46
Figure 38. Corrected crosshead strain of Sylgard sample cured at 25°C.	48
Figure 39. Corrected crosshead strain of Sylgard sample cured at 80°C.	48
Figure 40. Corrected crosshead strain of Sylgard sample cured at 120°C.	48
Figure 41. Corrected crosshead strain of Sylgard sample cured at 150°C.	49
Figure 42. Comparison of stress-strain relationships between crosshead and DIC data.	50
Figure 43. Strain field of PDMS in tension.	50
Figure 44. Slope of strain in x and y direction.	51
Figure 45. Poisson ratio as a function of strain in the y direction.	52

Figure 46. Shear strain as a function of strain in the y direction.....	53
Figure 47. Line scan half-way from top of region of interest (ROI).....	53
Figure 48. Strain in y-direction along the horizontal line half-way from top of ROI.	54
Figure 49. Strain in x-direction along the horizontal line half-way from top of ROI.	55
Figure 50. Strain profile for DIC and Crosshead techniques.....	56
Figure 51. Stress-strain relationship between DIC and Crosshead compression test data.....	57
Figure 52. Strain field of PDMS in compression	58
Figure 53. Slope of strain in x and y direction of compression Sylgard sample.....	59
Figure 54. Poisson ratio change as a function of strain in y direction.	59
Figure 55. Shear strain as a function of strain in the y direction.....	60
Figure 56. Line scan at half-way from top of region of interest (ROI).	61
Figure 57. Strain in y-direction along the horizontal line half-way from top of ROI.	61
Figure 58. Strain in x-direction along the horizontal line half-way from top of ROI.	62
Figure 59. Comparison of different strain measurement techniques.....	63
Figure 60. Stress-strain relationship of Sylgard samples in tension up to failure.	64
Figure 61. Stress-strain relationship of Gelest samples in tension up to failure	64
Figure 62. Typical failure PDMS sample under tension.....	66
Figure 63. Stress-strain relationship of Sylgard samples in compression up to failure.....	66
Figure 64. Stress-strain relationship of Gelest samples in tension up to failure.	67
Figure 65. Typical failure PDMS sample under compression.	68
Figure 66. Cure temperature effect on Young's modulus.....	69
Figure 67. Poisson ratio change with cure temperature.....	69
Figure 68. Effect of silica on compression modulus of Gelest samples.	71
Figure 69. Effect of silica on Poisson ratio of Gelest samples.....	71

LIST OF TABLES

Table 1: Different types of material formulation for Gelest.	17
Table 2: Effect of cure temperature on density of Sylgard™ samples.	21
Table 3: Effect of silica on density of Gelest™ samples.	22
Table 4. Glass transition temperatures for Sylgard samples taken from tan delta peaks	37
Table 5: Mechanical properties and characteristics of PDMS in tension.	65
Table 6: Mechanical properties and characterization of PDMS in compression.	67

ABSTRACT

Strain and displacement are critical parameters for mechanical characterization of materials. Measuring these parameters accurately can be challenging for hyper-elastic materials such as polydimethylsiloxane (PDMS) due to their non-linear deformation at strains above 30%. This restriction has led researchers to stick to application based modelling when it comes to using hyper-elastic materials in developing strain based sensors. This means that linear stress-strain relationship from 0-30% provides a predictable frame to design sensors using this material.

This thesis explores three different methods that can be used in measuring the strain of PDMS. The use of crosshead displacement, video extensometer and Digital Image Correlation (DIC) for strain measurement were compared. These three methods vary in complexity and cost to run. The most common method is the use of crosshead displacement since it is incorporated in the machine and hence does not require any additional devices to run an experiment. The next method is DIC which requires a digital single-lens reflex camera to take the images of the sample as it undergoes either a tension or compression test. It also requires the most amount of computation since the images taken have to be correlated using another software and the resulting strain matched to their corresponding stress from the raw data stored in the test machine. Lastly, it's by use of a video extensimeter. These methods are commonly used by researchers in the characterization of mechanical properties of hyper-elastic materials and therefore it would be prudent to compare their utility.

The focus will be mainly on DIC because more information about the material can be extracted from the data obtained from using this method. DIC analysis was done using both an open source Matlab code and commercial DIC software called LabJoy™.

Tension and compression PDMS samples were tested and their strain measurements analyzed to fully understand the material characteristics.

The PDMS used in this study was sourced from two different manufacturers. Sylgard 184 was purchased through a third party from Dow Corning. Tension and compression Sylgard samples were characterized as a function of five different temperatures, 25°C, 80°C, 100°C, 120°C and 150°C. The other manufacturer is Gelest Inc. They provided PDMS in five different components thereby giving us the flexibility to vary the actual PDMS contents. Silica was varied to give tension and compression samples containing 9%, 18%, 22% and 30% silica by weight.

In this research it was discovered that the gage section in tension samples experienced 20% more strain than what the crosshead records, the Poisson ratio was 0.46 and 0.61 for the tension and compression sample respectively. There was a 25% increase in the Young's modulus of the Sylgard when the cure temperature was changed from 25°C to 150°C tension sample and a 32% increase in the modulus of the Gelest compression sample when the silica was changed from 9% to 30%. The modulus of the compression sample increased by 61% with a 21% increase in silica, which indicated a 3:1 ratio.

In addition to mechanical characterization, thermal stability and viscoelastic material properties of PDMS were tested. Tan delta plots from dynamic mechanical analysis showed that the glass transition temperature of all the Sylgard samples cured at different temperatures were around -125°C. Thermogravimetric test showed that Sylgard undergoes one stage decomposition while Gelest undergoes a two stage decomposition.

The first stage is between 400°C and 600°C in both Sylgard and Gelest while the second stage in Gelest is between 550°C and 750°C.

CHAPTER 1: INTRODUCTION

The development of flexible sensors has become a wide area of research in recent years. The ability to embed a sensor in a flexible material has created numerous possibilities and applications. Traditional sensors, such as strain gages, would only be limited to a specific geometry while providing low strain measurements. Flexible sensors bring in adaptability, where the sensor can be attached to any geometry. They also have an extended range of strain that can be applied since the base material is stretchable [1]. Flexible sensors are typically comprised of two parts, a base material and an embedded electrical component. The base material is responsible for the mechanical property of the sensor while the electrical component is associated with resistance readings from the electrical input that the sensor is subjected to. The ideal base material for a flexible sensor should be capable of high strain measurements before failure [2].

Hyper-elastic materials are a special class of materials that respond elastically when they are subjected to very large strains. They show both a nonlinear material behavior as well as large shape changes. They can undergo large elastic deformations in order of around 100 to 700% that is fully recoverable meaning that the initial shape is recovered when load is removed [3]. They are nearly incompressible which means that when they are subjected to huge loads they change shape but overall volume remains almost constant. This also means that their Poisson's ratio is 0.5. Hyper-elastic materials are mostly used where high flexibility on a long run is required under large loads. The typical examples of their uses are as elastomeric pads in bridges, rail pads, car door seal and car tires [3].

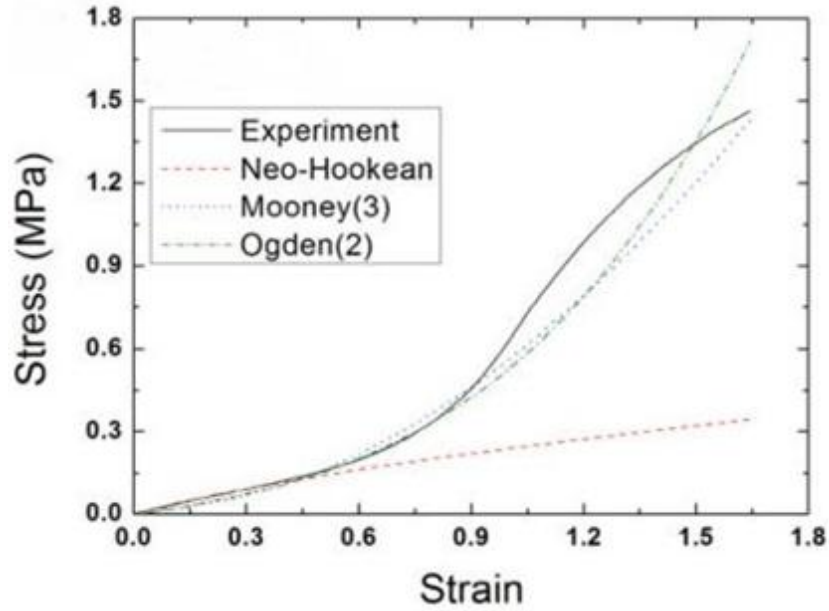


Figure 1. Nonlinear hyper-elastic models of PDMS [4].

From Figure 1, lower strain levels, $\sim 30\%$ and below, hyper-elastic materials can exhibit a linear behavior. It is this region of interest that researchers adhere to when developing flexible sensors. In this region, the modulus of the material can be calculated and the material constituent changed to obtain the desired material properties. As the development and application of strain based sensors increases, there has been an interest in the stress-strain behavior of hyper-elastic materials past the 30% strain threshold. It is this interest that led me to venture into the measurement of strain up to the point of failure. In addition, I also sought to extract more material characteristics below the 30% threshold.

Ogden 2nd order, Mooney 3rd order and Neo-Hookean are hyper-elastic models used to describe the non-linear stress-strain behaviour of complex materials such as rubbers, polymers, and biological tissue. These models assume that the material behaviour can be described by means of a strain energy density function, from which the

stress–strain relationships can be derived. In contrast to linear elastic materials, the stress-strain curve of a Neo-Hookean material is not linear. Instead, the relationship between applied stress and strain is initially linear, but at a certain point the stress-strain curve will plateau. The neo-Hookean model does not account for the dissipative release of energy as heat while straining the material and perfect elasticity is assumed at all stages of deformation [3].

1.1 Polydimethylsiloxane

Polydimethylsiloxane (PDMS) has become the most popular building material used in a variety of low-cost aqueous microfluidic devices aimed in particular at single use for biological or medical diagnostics. It is also suitable for the development of flexible sensors, flexible MEMs device, micro fluidics, and bio-MEMS. In order to have low power consumption, many groups use this material for the manufacture of mobile parts (often membrane, bridge...) in active systems such as micro valves and micro pumps [5].

PDMS is a mineral-organic silicon-based polymer of the siloxane family [5]. It is also known as Dimethicone and contains silicon, oxygen, and carbon [6]. In the last decade, the interest towards these kinds of materials has increased since they can be used in many different applications. The qualities that make it useful are its elastomeric properties, gas permeability, optical transparency, ease of bonding to itself and to glass, ease of molding, and relatively high chemical resistivity. In addition to those properties, the fact that it is inexpensive to be manufactured makes it noteworthy [7]. PDMS is considered inert, non-toxic and non-flammable [8]. Also, PDMS is biocompatible, so it is

appropriate to be used for prosthesis and internal body applications. PDMS has qualities that can be intermediate between an organic and an inorganic material.

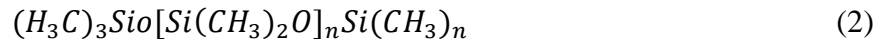
The PDMS molecules are highly flexible and they are arranged to form an amorphous material [9]. PDMS, such as the majority of polymers, forms amorphous solids because the process of crystallization is influenced by the topological constraints, such as the crosslinking, and by the difference length of the chains [10]. According to the molecular weight of the samples produced, PDMS presents a low volatility if the molecular weight is high and vice versa [11].

Polydimethylsiloxane is noteworthy and useful because it has a low surface tension, a moderate water interfacial tension and no surface viscosity. They can be found in a wide variety of configurations and they present a low activation energy for the viscous flow. In addition to that, PDMS have low glass transition temperature, low boiling points (oligomers), low freezing and pour point and high compressibility. In the environment, they present a low level of hazard, also because of the low flammability, and they are well resistant to the weather. PDMS show high permeability to gas and low molecular weight and a large free volume [12]. Some of the properties described before are only valid for polymer solution, while others are applicable only for chemical cross-linked gels.

Hereafter, the empirical, the chemical and the structural formula of the PDMS will be presented. The empirical formula shows the simplest number ratio of atoms of the elements presents in the compound. Instead, the chemical formula shows how many atoms of each element are present in the compound. With the structural formula, instead, the structure of the molecule is shown. The empirical formula PDMS:



The value of n can influence the state of the PDMS. If n , the number of times that the monomers repeated, is low; then the PDMS will be liquid. If n is high, it will be semi-solid [13-14]. The chemical formula of the Polydimethylsiloxane instead is:



The structural formula of the PDMS is shown in Figure 2. [11]

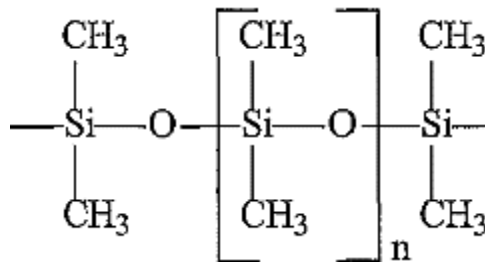


Figure 2. Chemical Structure of PDMS [8].

Since it is a polymer, in the structure, there will be a monomer unit ($[(CH_3)_2]$) repeated n -times [11]. A 3D model of the fundamental chemical structure of a Polydimethylsiloxane molecule is shown in Figure 3.

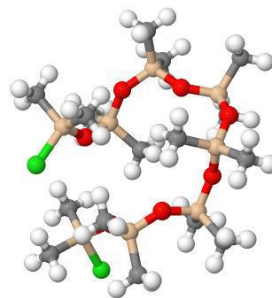


Figure 3. 3D structure of a PDMS molecule [14].

Polymers such as the Polydimethylsiloxane have characteristics halfway between solid and liquid materials. The complexity in measuring their properties comes from their unique texture and consistency. In particular, the consistency of this semi-solid, sticky and viscous material makes it challenging to measure its properties. It is possible to measure them with a macroscopic or microscopic approach. In this thesis, only the microscopic one is used.

1.2 Strain measurement

Strain measurement below the 30% threshold brings in the issue of accuracy because different methods can be used to measure the strain field. Even though the strain field below 30% is linear, the method of strain measurement will determine the accuracy of the values reported. In order to report accurate values for the failure strain, Young's modulus and Poisson's ratio, the measurements of strain should be done to a high degree of confidence.

Typical methods of strain measurements include the use of crosshead where the displacement readings obtained directly from the measuring instrument as load is applied. This method is common because it does not require any additional equipment to measure a specific part of the sample. The second is the use of a video extensometer that tracks a pair of dots marked on the sample to give a more accurate strain measurement. Lastly, use of DIC which gives a full field strain measurement and local strain patterns from the numerous dots that have been sprinkled on the sample.

Most of the mechanical characterization of PDMS has been done through the manual measurement of its properties with a heavy reliance on Finite Element Methods. F Schneider, T Fellner, J Wilde and U Wallrabe [15] in their characterization of silicones

for MEMS, manually measured the displacement of a PDMS sample in tension and used a correction factor from FEM modeling to correct it. The manual measurement was done by recording the displacement in the gage section after each subsequent loading. The difference between the crosshead strain reading and the manual measured was by a factor of 0.5. This value was verified by FEA methods. The tests that followed were done using the crosshead and their strain values corrected by a factor of 0.5. This factor comes into play because the strain recorded by the testing machine is inclusive of the wider section of the dogbone sample. Unlike the narrow gage section, the wide section does not experience uniform strain therefore it does not represent the real material behavior.

The last method is strain measurement using Digital Image Correlation (DIC) which is an optical method measuring the full-field surface displacement of an object by comparing the images before and after deformation. The displacement components are readily to be observed. DIC was firstly introduced in 1980s as a measure of displacement components in laser speckle metrology by W.F.Peters and W.H.Ranson of University of South Carolina [16]. Peters and Ranson utilized a cross-correlation algorithm to correlate a subset of pixels between the reference and deformed images. In the following years, digital image correlation technique has been highly developed in increasing the correlation speed, improving the correlation accuracy and so forth. Most of the efforts focused on the improvement of the correlation algorithms. For example, the bilinear interpolation method, Newton-Raphson numerical solution method, coarse-fine search method and so on [17]. In recent years, DIC has been employed in various problems and it is found ideally suitable for fracture mechanics investigation, high temperature deformation analysis and so on. It has been widely used in experimental mechanics.

DIC has been used to precisely determine the Poisson ratio of soft materials. The Poisson ratio of PDMS has been reported to be around 0.5 [18]. The samples were tested at a crosshead speed of 7mm/s up to 10% strain. A Canon 550D DSLR camera fitted with a Canon 100mm macro lens was used to take the pictures that were later correlated using a commercial software known as MatchID.

1.3 Digital Image Correlation

Digital image correlation (DIC) is an optical method to measure deformation on an objects surface. This usually occurs in three steps. Images of a surface are analyzed over time, a cross correlation technique is used to determine displacement and then strain is calculated from the displacement. DIC provides a non-contact strain measurement method which does not interfere with the material while being tested. It also gives a full-field data by tracking hundreds of tiny dots sprayed on the sample thereby giving a clear strain field.

The measurement of displacements and displacement gradients has always been an important topic in the evaluation of material properties, such as material strengths or fracture parameters and in experimental stress analysis. Optical techniques such as moiré interferometry [19], holography [20], and speckle interferometry [21] have been proven to be matured techniques to analyze macroscopic parameters and are being applied successfully in many different applications. However, all the interferometric techniques have stringent requirements for system's stability. Moreover, the processing of fringe patterns is laborious and time-consuming. This technical difficulty has raised many researchers' attention and computerized procedures [22] have been developed to automate the processing of the data from the fringe patterns.

In the last decade, a non-contacting optical technique, digital image correlation, has been developed by S. R Sutton and Bruck H. A [23-25]. It was applied to measurement of displacements and strains. The applications include microscopic strain measurements in electronic packaging [26], strain fields in polyurethane foam plastic materials and evaluation of their mechanical properties [27] and evaluation of thermal strain in the solder joints [28]. This computer vision technique has the advantages of a simple system and direct sensing and thus avoids the laborious interpretation of interferometric fringes.

1.4 Outline

This thesis will look into mechanical characterization of PDMS using non-contact strain measurement techniques. The emphasis is on the DIC technique and as such the theory behind the technique. The theory behind DIC will be explained followed by the material preparation and the different characterizations tests such as Dynamic Mechanical Analysis and Thermogravimetric Analysis. Mechanical testing equipment and procedure will follow giving way to the results and discussion of all the tests that were carried out. A brief summary is given at the end with future work recommendations.

CHAPTER 2: THEORY OF DIC

2.1 Introduction

DIC works by dividing the surface image into subsets-series of boxes with a recognizable pattern in each. A correlation technique is then used to analyze how each subset has moved and deformed during the test. Finally, the displacement for each subset is calculated and the local strain data is derived from the displacement vectors. These steps are repeated for each subset over the entire surface. The objective of this chapter is to discuss the mathematical approach behind DIC.

2.2 Methodology

In principle, DIC compares a series of grey-scale images of a sample at different stages of deformation, tracks pixels movement in the region of interest (ROI) [29] and calculates displacement and strain by the use of correlation algorithm.

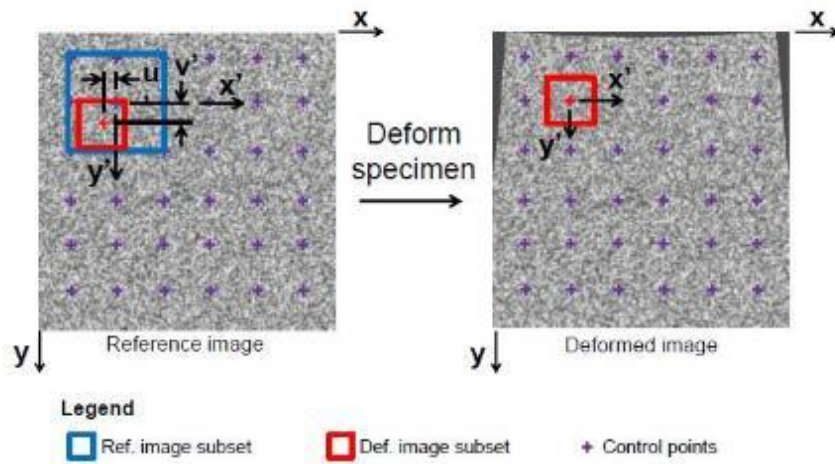


Figure 4. Schematic of digital image correlation methodology [29].

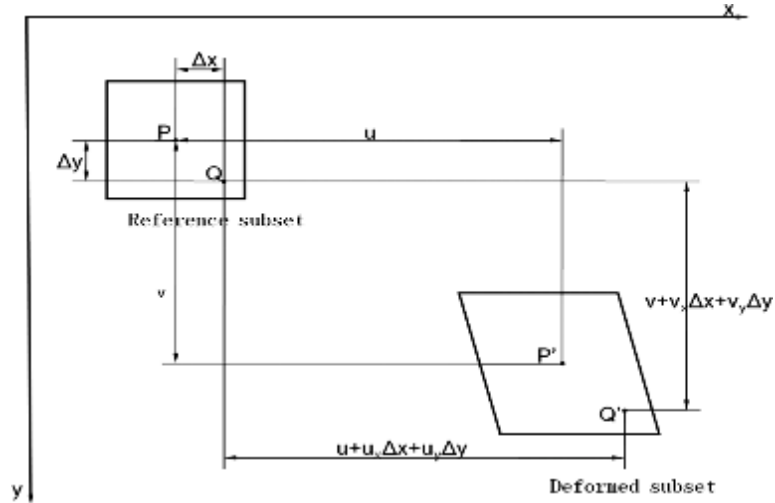


Figure 5. Subset before and after deformation [29].

In Figure 4 above, a grid of control points (purple crosses) is defined over the region of interest. The normalized cross-correlation coefficient is computed by convolving a subset in the deformed image (red box) with the corresponding larger subset in the reference image (blue box). The actual displacement (u,v) is the displacement that maximized the correlation coefficient. In Figure 5 the grid moves during the deformation, and original grid boundary will also deform to cover all the original pixels within the grid, so coordinates for all pixels will change, for example, the center of the grid has an original coordinate of (x, y) , after deformation it changes to (x^*,y^*) .

Let u be u_0 and v be v_0 be The displacement of P is represented as u_0 in x direction and v_0 in y direction. So, the following equation can be found:

$$\begin{aligned} x'_0 &= x_0 + u_0 \\ y'_0 &= y_0 + v_0 \end{aligned} \quad (3)$$

We now assume $Q(x_o, y_o)$ is a random selected point other than Q within the subset and the location of Q relative to P can be expressed as:

$$\begin{aligned}x_Q &= x_Q + \Delta x \\y_Q &= y_Q + \Delta y\end{aligned}\quad (4)$$

In the above expression, Δx and Δy are the distance from P to Q in the horizontal and vertical direction. After deformation, $Q(x_Q, y_Q)$ moved to $\hat{Q}(x_Q, y_Q)$

$$\begin{aligned}x_{Q'} &= x_Q + u_Q \\y_{Q'} &= y_Q + v_Q\end{aligned}\quad (5)$$

Where, u_Q and v_Q are distances of $\hat{Q}(x_Q, y_Q)$ with respect to $Q(x_Q, y_Q)$ in x and y direction. For rigid body translation, u_Q and v_Q are equal to u_o and v_o respectively. However, the corresponding subset in deformed image is not necessarily identical to the defined square subset in the reference image. Once the object is subjected to deformations other than rigid body translation, for example, shear, rotation, compression and tension, the subset possibly deforms and presents as a different shape. In this case, as u_Q and v_Q are no longer equal to u_o and v_o , in order to describe the shape of the deformed subset, first-order Tylor series expansion in terms of Δx and Δy can be utilized. Here, assuming that Δx and Δy are small such that u_Q and v_Q can be approximated:

$$\begin{cases}u_Q = u_o + \frac{\partial u_o}{\partial x} \Delta x + \frac{\partial u_o}{\partial y} \Delta y \\v_Q = v_o + \frac{\partial v_o}{\partial x} \Delta x + \frac{\partial v_o}{\partial y} \Delta y\end{cases}\quad (6)$$

By substituting Equation 6 in Equation 5, $\hat{Q}(x_Q, y_Q)$ can be expressed as:

$$\begin{cases} x'_Q = x_Q + u_0 + \frac{\partial u_0}{\partial x} \Delta x + \frac{\partial u_0}{\partial y} \Delta y \\ y'_Q = y_Q + v_0 + \frac{\partial v_0}{\partial x} \Delta x + \frac{\partial v_0}{\partial y} \Delta y \end{cases} \quad (7)$$

The center of the subset after deformation, P' , can be expressed in terms of u , v , and $\frac{\partial u}{\partial x}$, $\frac{\partial v}{\partial x}$, $\frac{\partial u}{\partial y}$ and $\frac{\partial v}{\partial y}$.

$$\begin{cases} x' = x + u + \frac{\partial u}{\partial x} \Delta x + \frac{\partial u}{\partial y} \Delta y \\ y' = y + v + \frac{\partial v}{\partial x} \Delta x + \frac{\partial v}{\partial y} \Delta y \end{cases} \quad (8)$$

The deformation of the subset can be described as Equation. 8 where u and v donate the displacements in integer pixels, $\frac{\partial u}{\partial x}$, $\frac{\partial v}{\partial x}$, $\frac{\partial u}{\partial y}$ and $\frac{\partial v}{\partial y}$ are displacement gradients related to the subset deformation. The six parameters are adjusted through the algorithm to find the region in the deformed image best match the defined subset in the reference image [30]. In this project, based on the theory stated above, the correlation is implemented by MATLAB using the normalized 2D cross-correlation as the core algorithm [30].

A commercial DIC software, LabJoy®, was used to analyze the bulk images from the samples while a MatLab code was used to analyze the local strain patterns of the samples. There is no public information on how LabJoy® uses a core algorithm for cross-correlation. However, in the Matlab code the heart of the correlation process is in the *cpcorr mod.m* function, a slightly modified version of the standard function in the Image Processing Toolbox *cpcorr.m*, written by Matlab. The code can be found in Appendix A.

For each control point, the code takes a subset of pixels around the control point in the deformed image, and a larger subset (generally twice as big) around the corresponding control point in the reference image, as shown in Figure 4. The size of the

reference subset with respect to the deformed subset is controlled by the search zone. Increasing the search zone will increase the maximum allowable displacement, but at the cost of a larger border around the region of interest in which control points cannot be correlated and increased computation time. The code computes the normalized cross-correlation coefficient, C , [31] for a range of theoretical displacements, (u', v') , in 1 pixel increments by convolving the subset from the deformed image with the larger subset from the reference image according to

$$C(u', v') = \frac{\sum_{x', y'} [(r(x', y') - \bar{r}_{u', v'}) (d(x' - u', y' - v') - \bar{d})]}{\left\{ \sum_{x', y'} [(r(x', y') - \bar{r}_{u', v'})^2] \sum_{x', y'} [(d(x' - u', y' - v') - \bar{d})^2] \right\}^{1/2}} \quad (9)$$

where r is the intensity of the pixels in the reference subset, d is the intensity of the pixels in the deformed subset, and (x', y') are local subset coordinate axes whose origin is at the control point at the subset center. If the value of the computed correlation coefficient at a given control point is less than the value set for the threshold, the correlation is determined to be poor and no data is returned for that control point. By decreasing the threshold value, the user can allow more grid points to be correlated, but at the expense of having less certainty in the validity of the correlations.

In order to calculate displacements to within 1/100 of a pixel, the nine discrete correlation coefficients surrounding the absolute maximum coefficient are interpolated using a second order polynomial in u' and v' . The actual displacement $(u; v)$ for a control point is the theoretical displacement $(u_0; v_0)$ corresponding to the maximum interpolated correlation coefficient. The output of the code is discrete displacement values for each

control point for each image. These displacements can then be translated to strain by calculating their rate of change.

CHAPTER 3: EXPERIMENTAL METHOD

This chapter discusses material preparation for Gelest and Sylgard and different mechanical characterization test. The tests include density measurement, dynamic mechanical analysis and thermogravimetric analysis. This chapter also discusses mechanical testing procedures for tension and compression that were followed to obtain strain measurements from the PDMS samples.

3.1 Material Preparation

Sylgard™ 184 samples were made by manually mixing Part A (dimethylvinyl-terminated) and Part B (methylhydrogen siloxane), shown in Figure 6, at a ratio of 10:1 respectively. The mixture was then poured onto the bottom part of the mold shown in Figure 6 and placed in a vacuum chamber for an hour to remove the bubbles after which it is covered and set to cure at different temperatures for five different sets 25°C, 80°C, 100°C, 120°C and 150°C for three hours. Lastly the sample is removed from the mold and placed in the oven to post cure at 180°C.



Figure 6. PDMS Sylgard® 184 Kit with Part A and Part B [32].

Gelest™ samples were made by mixing a polymer (vinyl terminated polydimethylsiloxane), a crosslinker (methylhydrosiloxane), silica (silicon dioxide) and a catalyst (platinum-cyclovinylmethylsiloxane complex). The formulation is shown in Table 1 below. Four sets of samples were made. The polymer is mixed with the silica, then the cross linker is manually mixed with the mixture, finally a catalyst is introduced at 200 parts per million. The mixture was then poured onto the bottom part of the mold and placed in a vacuum chamber for an hour to remove the bubbles after which it is covered and set to cure at 80°C for three hours. Lastly the sample is removed from the mold and placed in the oven to post cure at 180°C.

Table 1: Different types of material formulation for Gelest.

SAMPLE NAME	BASE POLYMER	CROSSLINKER	CATALYST (parts per million)	SILICA CONTENT
Gelest 10:1	7%	4%	200	9%
Gelest 10:2	80%	4%	200	16%
Gelest 10:3	74%	4%	200	22%
Gelest 10:4	66%	4%	200	30%



Figure 7. (a) Compression sample mold (b) Tension sheet mold.

The compression sample is a 10mm cube made using an aluminum mold with a series of six slots as shown in Figure 7. (a). The tension mold shown in Figure 6. (b) consists of two square aluminum sheets 4 mm thick and 270 mm wide. The window of the shim on the mold measures 125 mm by 139 mm. This measurement ensures the sample made will be enough to cut out five dog bone samples. The two square aluminum sheets are covered by a 50 μ m thick thermalimide high performance bagging film which can sustain cure temperatures up to 426°C.

The film is used because PDMS easily peels away from it after curing and so there is no need for mold release. The film was taped using an EconoTape 1 from Airtech International Inc. which has a maximum temperature use of 177°C. The sheet from the tension mold was cut according to ASTM D-412-C die standard as shown in Figure 8. The die ensures that the all rubber materials tested by researchers have the same dimensions therefore the reported results from various tests can be easily accepted.

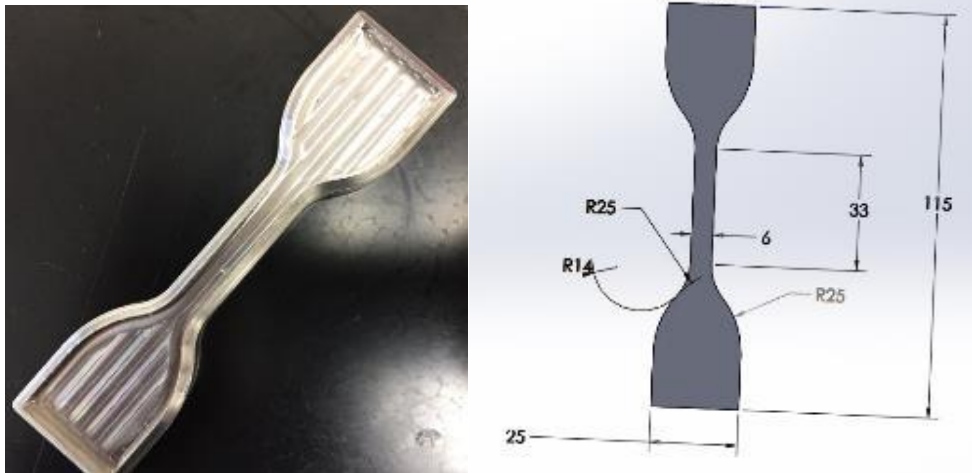


Figure 8. (a) ASTM D412-C Tension die (b) ASTM D412-C dimensions.

Figure 9 below shows a tension sample used with a video extensometer, a tension sample used to take DIC measurements and a compression sample used to take DIC strain measurements respectively.

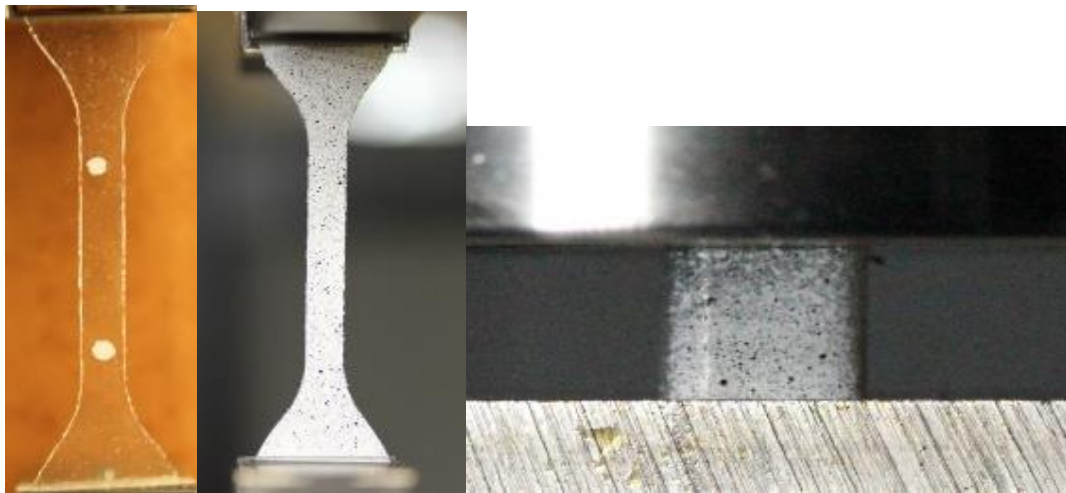


Figure 9. (a) Video Extensometer Tension Sample (b) DIC Tension Sample (c) DIC Compression Sample.

3.2 Material Characterization

3.2.1 Density

Gas pycnometry is recognized as one of the most reliable techniques for obtaining true, absolute, skeletal, and apparent volume and density. This technique is non-destructive as it uses the gas displacement method to measure volume. Inert gases, such as helium or nitrogen, are used as the displacement medium. Density calculations using the gas displacement method are much more accurate and reproducible than the traditional Archimedes water displacement method [33]. A gas pycnometer operates by detecting the pressure change resulting from displacement of gas by a solid object. Expanding a quantity of gas at known pressure into an empty chamber and measuring the pressure establishes a baseline. Then a sample is placed in the chamber and the chamber is resealed. The same quantity of gas at the same pressure is again expanded into the sample chamber, and the pressure is measured. The difference in the two pressure combined with the known volume of the empty sample chamber allows the volume of the sample to be determined using the gas law [33].



Figure 10. AccuPyc II micromeritics™.

The AccuPyc II micrometrics™ pycnometer, shown in Figure 10 above, takes the mass of the sample that is placed in the chamber and runs a few cycles measuring the density of the sample. This technique uses the gas displacement method to measure volume accurately. An inert gas, nitrogen, is used as the displacement medium. The sample is sealed in the instrument compartment of known volume, the appropriate inert gas is admitted, and then expanded into another precision internal volume. The pressures observed upon filling the sample chamber and then discharging it into a second empty chamber allow computation of the sample solid phase volume. Helium molecules rapidly fill pores as small as one angstrom in diameter; only the solid phase of the sample displaces the gas. Dividing this volume into the sample weight gives the gas displacement density [34].

Table 2: Effect of cure temperature on density of Sylgard™ samples.

SAMPLE	CURE TEMPERATURE (°C)	DENSITY (g/cc)
Sylgard 25	25	1.19±0.01
Sylgard 80	80	1.20±0.01
Sylgard 100	100	1.19±0.02
Sylgard 120	120	1.15±0.02
Sylgard 150	150	1.17±0.02

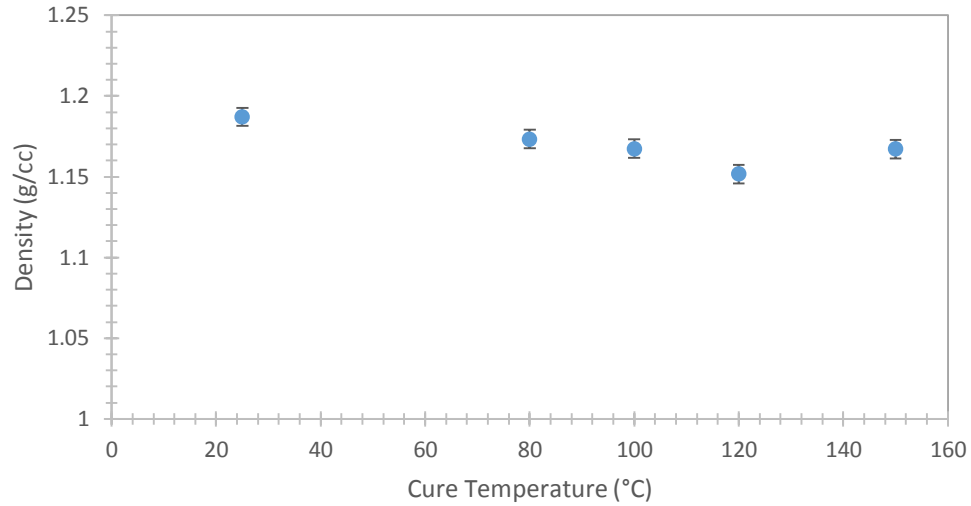


Figure 11. Effect of cure temperature on density of Sylgard™ sample.

The Gelest™ and Sylgard® samples densities were tested using a gas pycnometer shown in Figure 10. Literature review revealed that most researchers use a density of 1.03 g/cc provided by the manufacturer Dow Corning for Sylgard™ samples [32]. The density of two 6061 aluminum blocks was measured using the pycnometer. The density was found to be 2.71 ± 0.12 g/cc which is exactly what is recorded by Alcoa© which is the world leader in aluminum manufacturing [18]. The average density for all the Sylgard® samples was 1.1788 g/cc. This is 14% more than what is reported by the manufacturer. It was also discovered that the density is unaffected by the cure temperature of the Sylgard® samples.

Table 3: Effect of silica on density of Gelest™ samples.

SAMPLE	CURE TEMPERATURE(°C)	DENSITY (g/cc)
Gelest 10:1	80	1.22 ± 0.02
Gelest 10:2	80	1.25 ± 0.06

Gelest 10:3	80	1.29±0.02
Gelest 10:4	80	1.33±0.02

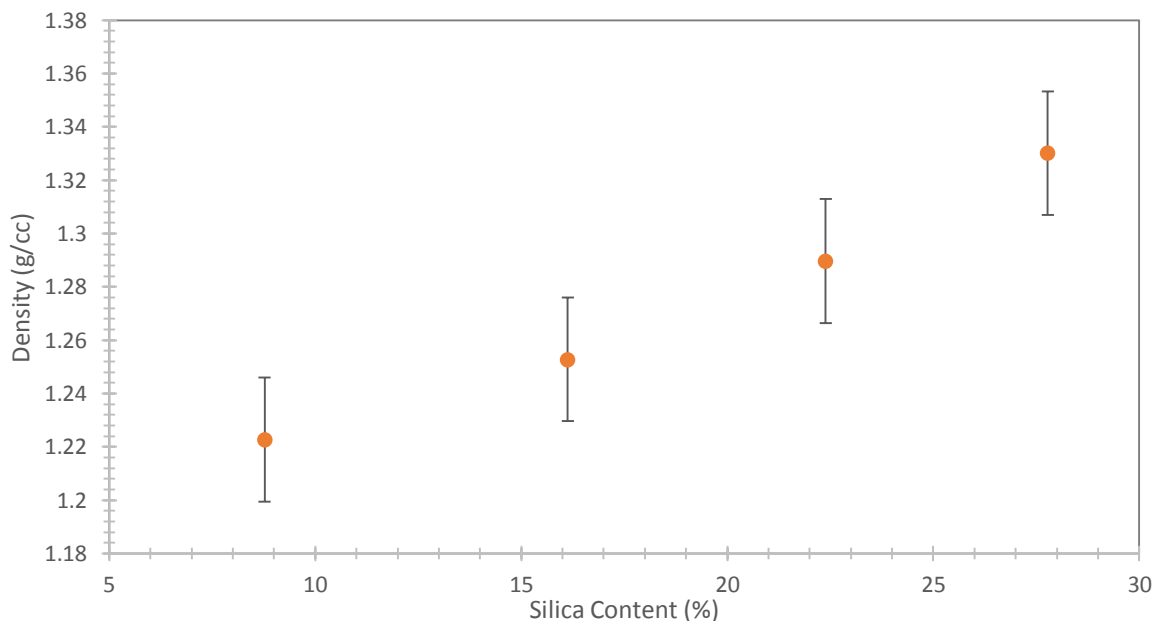


Figure 12. Effect of silica on density of Gelest™ samples.

The density measurement of Gelest™ samples show a steady increase in density with an increase in silica. There was a 5.5% increase in density corresponding to a 233.3% increase in silica from the Gelest™ 10:1 which has ~9% silica to Gelest™ 10:4 which has ~30% silica. Although the increase in density is marginal compared to the increase in silica, there is certainly a significant linear trend associated with an increase in silica in Gelest™ samples.

3.2.2 Dynamic Mechanical Analysis

A Dynamic mechanical analysis (DMA) was performed on the Sylgard® 184 samples cured at different temperatures to better understand their viscoelastic behavior.

DMA is a thermal analysis technique that measures the properties of materials as they are deformed under periodic stress. In DMA a variable sinusoidal stress is applied, and the resultant sinusoidal strain is measured. If the material being evaluated is purely elastic, the phase difference between the stress and strain sine waves is 0° . If the material is purely viscous, the phase difference is 90° .

However, most real-world materials including polymers are viscoelastic and exhibit a phase difference between those extremes. This phase difference, together with the amplitudes of the stress and strain waves, is used to determine a variety of fundamental material parameters, including storage and loss modulus, $\tan \delta$, complex and dynamic viscosity, storage and loss compliance, transition temperatures, creep, and stress relaxation, as well as related performance attributes such as rate and degree of cure, sound absorption and impact resistance, and morphology [35]

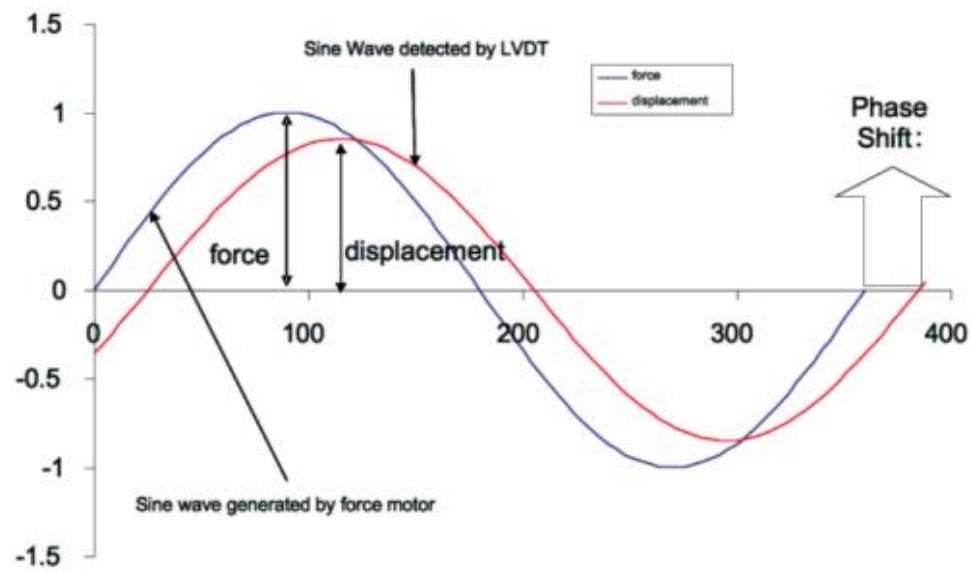


Figure 13. The relationship of the applied sinusoidal stress to strain is shown, with the resultant phase lag and deformation [36].

For an applied stress varying sinusoidally with time, a viscoelastic material will respond with a sinusoidal strain for low amplitudes of stress. The sinusoidal variation in time is usually described as a rate specified by the frequency ($f = \text{Hz}$; $\omega = \text{rad/sec}$). The strain of a viscoelastic body is out of phase with the stress applied, by the phase angle, δ . This phase lag is due to the excess time necessary for molecular motions and relaxations to occur. Dynamic stress, σ , and strain, ε , given as:

$$\sigma = \sigma_0 \sin(\omega t + \delta) \quad (10)$$

$$\varepsilon = \varepsilon_0 \sin(\omega t) \quad (11)$$

where ω is the angular frequency. Using this notation, stress can be divided into an “in phase” component ($\sigma_0 \cos(\delta)$) and an “out-of-phase” component ($\sigma_0 \sin(\delta)$) and rewritten as:

$$\sigma = \sigma_0 \sin(\omega t) \cos \delta + \sigma_0 \cos(\omega t) \sin \delta \quad (12)$$

Dividing stress by strain to yield a modulus and using the symbols E1 and E2 for the inphase (real) and out-of-phase (imaginary) moduli respectively yields: where E1 is $(\sigma_0/\varepsilon_0) \cos \delta$ and E2 is $(\sigma_0/\varepsilon_0) \sin \delta$. Therefore, in complex notation:

$$E^* = E1 + iE2 \quad (13)$$

E1 is referred to as the storage modulus and E2 as the out of phase modulus. The phase angle δ can be written as

$$\tan \delta = E_2/E_1 \quad (14)$$

Equation (13) shows that the complex modulus obtained from a dynamic mechanical test consists of “real” and “imaginary” parts. The real (storage) part describes the ability of the material to store potential energy and release it upon deformation. The imaginary (loss) portion is associated with energy dissipation in the form of heat upon deformation. The storage modulus is often times associated with “stiffness” of a material and is related to the Young’s modulus, E. The dynamic loss modulus is often associated with “internal friction” and is sensitive to different kinds of molecular motions, relaxation processes, transitions, morphology and other structural heterogeneities. Thus, the dynamic properties provide information at the molecular level to understanding the polymer mechanical behavior [35].

Modulus values change with temperature and transitions in materials can be seen as changes in the storage modulus or tan delta curves. This includes not only the glass transition and the melt, but also other transitions that occur in the glassy or rubbery plateau as shown in Figure 14 below.

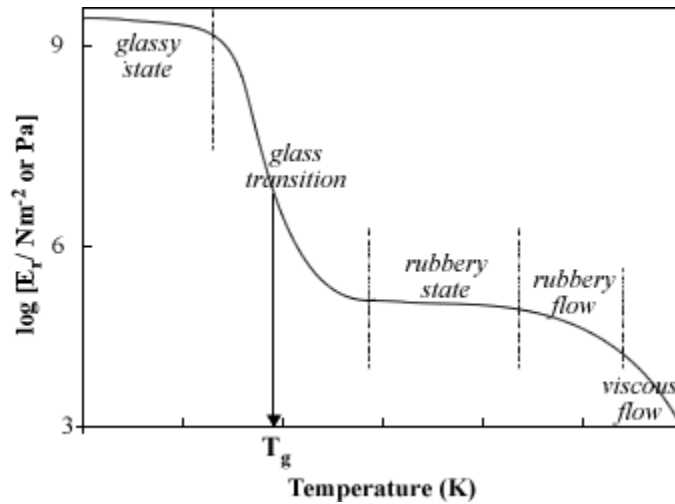


Figure 14. Modulus values change with temperature and transitions in materials [36].

In general, transitions in materials are associated with different localized or medium-to long-range cooperative motions of molecular segments. The glass transition is associated with cooperative motion among a large number of chain segments, including those from neighboring polymer chains [37]. Although there are several thermal techniques available to make T_g (glass transition temperature) measurements, by far the most sensitive technique is dynamic mechanical analysis.

After scanning the sample under test, the viscoelastic moduli, storage and loss modulus, damping properties, and tan delta, parameters can be used to define the T_g . T_g using tan delta peak which occurs at the highest temperature and is used historically in literature. It is a good measure of the ‘leather like’ midpoint between the glassy and rubbery states of a polymer. The height and shape of the tan delta peak change systematically with amorphous content. The parameter used to detect the glass transition is usually reported along with the frequency of oscillation, the temperature ramp rate, the clamp type used, and the sample dimensions [38].

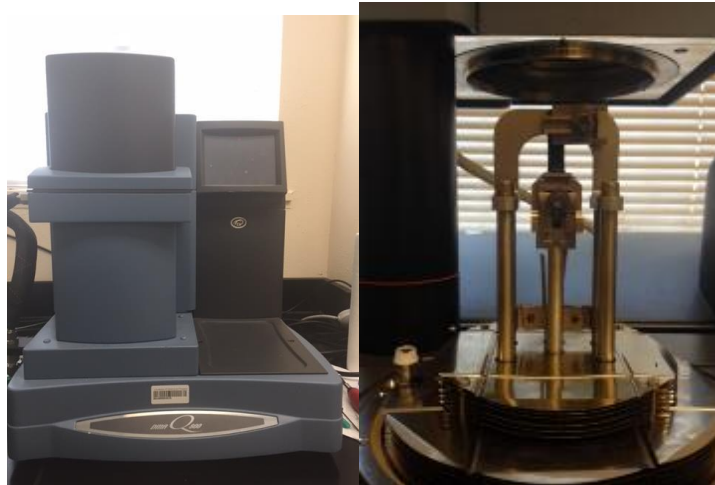


Figure 15. Sylgard® sample in tension ready for DMA test.

3.2.3 Thermogravimetric Analysis

This technique measures the thermally induced weight change of a material as a function of temperature in a controlled environment. The measurements are used to primarily determine the composition of material and to predict their thermal stability at temperatures up to 1000°C. Characterization of material can be done depending on weight loss or gain due to decomposition, oxidation or dehydration. The following information can be extracted from a thermogravimetric analysis: thermal stability of materials, oxidation stability of materials, composition of multi-component systems, decomposition kinetics of materials, effect of corrosive or reactive atmospheres on materials and moisture and volatiles content of materials.

The weight loss by the sample can be either due to thermal decomposition with the formation of gaseous reaction product as chemical bonds break, evaporation as loss of volatiles with elevated temperature, reduction from interaction of the sample with the reducing atmosphere and desorption. Weight gain can be due to oxidation due to interaction of the sample with an oxidizing atmosphere or absorption.



Figure 16. TA Q100 Thermogravimetric Analysis Instrument.

3.3 Mechanical Testing

All tension samples were tested at a strain rate of 10% per minute and all the compression samples were tested at a strain rate of 20% per minute. This gives a common basis of comparison among the three methods of strain measurements. The strain rates were chosen after running multiple tests to determine the best strain rate that the camera can fully capture the deformation from the sample on an image.

For the DIC technique a Canon® EOS Rebel T5 camera is placed perpendicular to the sample that is mounted on the Instron Single Column Machine. The camera has an image sensor having approximately 18 effective megapixels and 18.70 total megapixels. The pixel unit is 4.3 μm and the aspect ratio is 3:2 (Horizontal: Vertical) [39]. It is paramount that the camera is leveled with the machine and that it is perpendicular to the sample to ensure that the images taken are not askew. Even a 1° offset will translate into an inaccurate correlation from the DIC software. This inaccuracy is easily carried through to the subsequent images leading to an overall misrepresentation of strain patterns and passion ratios. Thus, we assume the sample is planar, parallel to and at a constant distance from the visual sensor during the entire experiment. The sample itself has black dots sprinkled on a white background, this contrast is what assists the DIC software, LabJoy™, in pattern recognition and correlation. The software is able to track the changes in position of the black dots on the white background on the face of the sample.



Figure 17. (a) PDMS sample setup in tension (b) Instron Single Column Machine (c) Canon® EOS Rebel T5 Camera[38].

Strain patterns and Poisson ratio values once obtained can be matched with the corresponding load from the raw data, this gives a complete picture of what the material experienced. In running the experiment, a base image is taken, this will be the ‘zero’ image from which the correlation will be based upon. The tension/compression test is started and an image is taken after 6 seconds for tension and 5 seconds for compression. The tests were run up to 30% strain, beyond that the error associated with relating batches of images at a time was significant and was carried through every batch. For the purposes of material characterization, the Poisson ratio and Young’s Modulus can be accurately reported from DIC data that spans up to a strain of 30%.

In addition to DIC experiments, a video extensometer with a 400mm field of view was used to capture the strain of tension samples. DIC can only accurately track changes in displacement up to 30% strain before the errors accumulating from subsequent image correlation diminish the accuracy of the strain recorded. The video extensometer is able to track the strain in a sample up to failure. This has the advantage of giving a complete and accurate picture of what the material experiences until it fails. Two white dots, one inch

apart, are impressed on the gage section of the sample using a stencil. The sample is then mounted perpendicular to the video extensometer. The video extensometer illuminates a red color which assists in spotting the two white dots on the data acquisition software on the computer. This setup is shown in Figure 18 below.

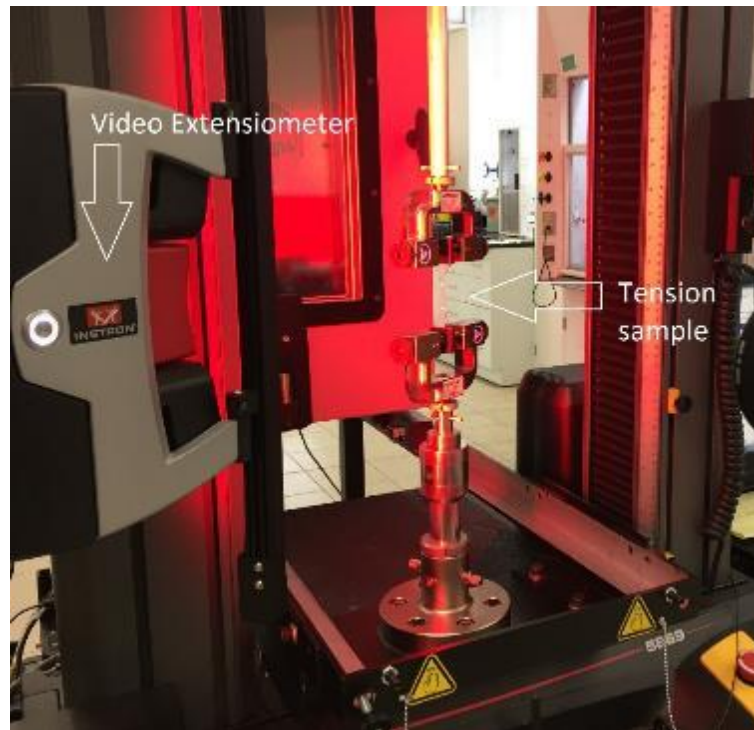


Figure 18. Video extensometer setup.

All tension samples were tested at a strain rate of 10% per minute and all the compression samples were tested at a strain rate of 20% per minute. The strain rates were chosen after running multiple tests to determine the best strain rate that the camera can fully capture the deformation. These strain rates corresponded to well detailed images that were able to be correlated using the DIC software.

CHAPTER 4: RESULTS AND DISCUSSION

This chapter will discuss the results from mechanical tests and material characterization. The discussion will focus on the glass transition temperature from the DMA analysis, residual mass from the TGA tests, strain patterns from the FEA, Poisson ratio from DIC tests and effects of silica and cure temperature on PDMS.

4.1 Dynamic Mechanical Analysis

Liquid nitrogen was used to test the samples from a temperature of 25°C to a temperature of -140°C. The samples tested were rectangular in shape, measuring 10mm in width, 25mm in length and 1.2mm in thickness. The test was run using tension clamps, at a frequency of 1 Hz, a load of 1N, an amplitude of 10 microns, and a ramp rate of 5°C/min. The storage modulus, loss modulus and tan delta plots were analyzed.

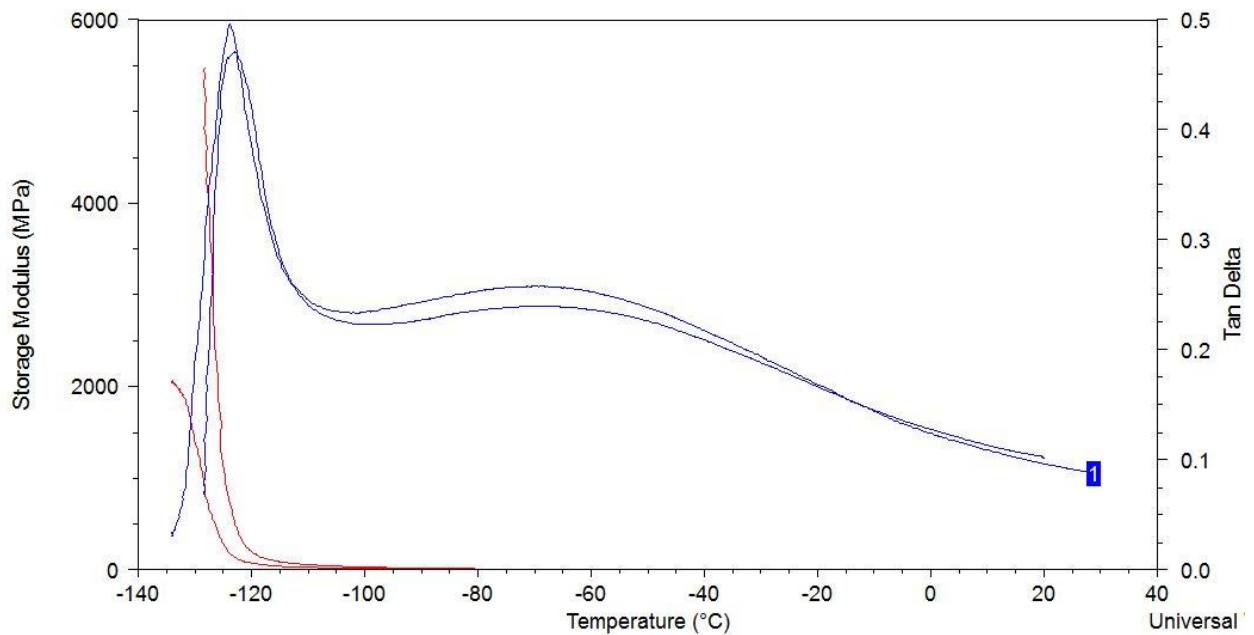


Figure 19. Storage modulus and tan delta as a function of temperature of Sylgard sample cured at 25°C.

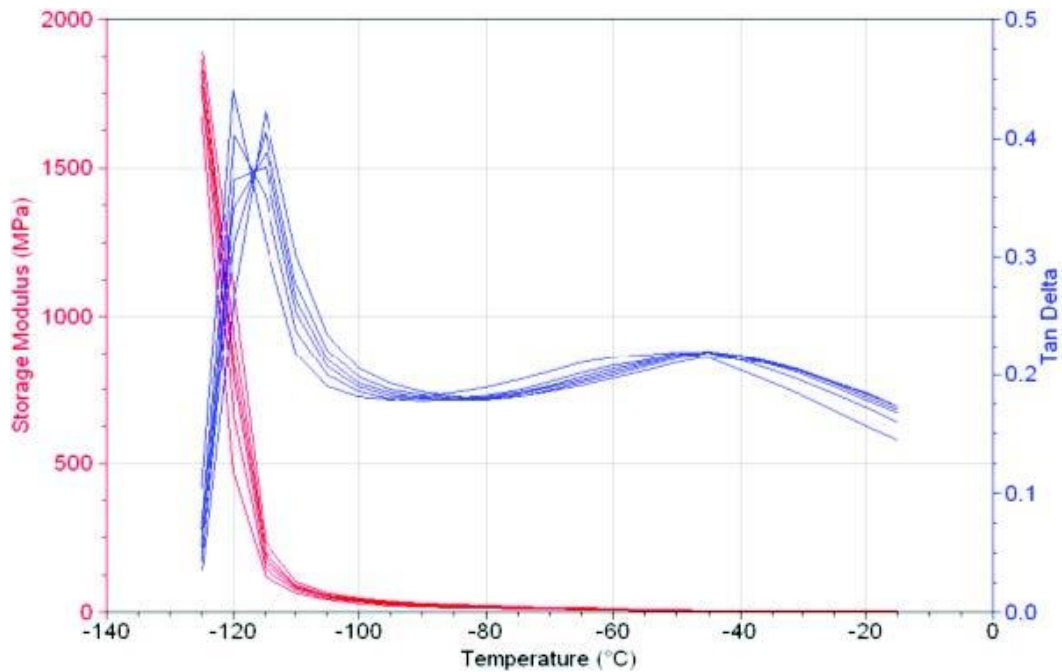


Figure 20. Published storage modulus and tan delta as a function of temperature for Sylgard 184 [40].

Figure 20 is from literature where a complete DMA analysis of PDMS was published. The results of the storage modulus and tan delta are very comparable to the results for Sylgard 25. This led us to believe that the sample was cured at room temperature. From Figure 20 the storage modulus decreases monotonically with temperature for polymer relaxation [40].

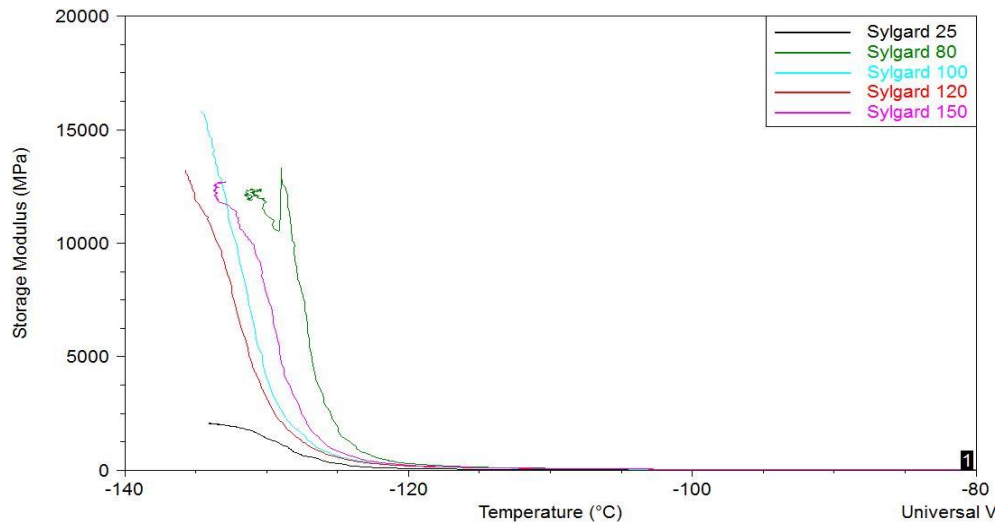


Figure 21. Storage modulus as a function of temperature for Sylgard samples cured at different temperatures.

Figure 21 shows the storage modulus of the rest of the samples. There is a clear indication that the cure temperature affects the rate at which the polymer relaxes as temperature is increased. However, there is no clear trend with regard to the cure temperature. Sylgard 80 has the steepest gradient followed by Sylgard 150. There is no known literature about the effects of cure temperature on the relaxation gradient.

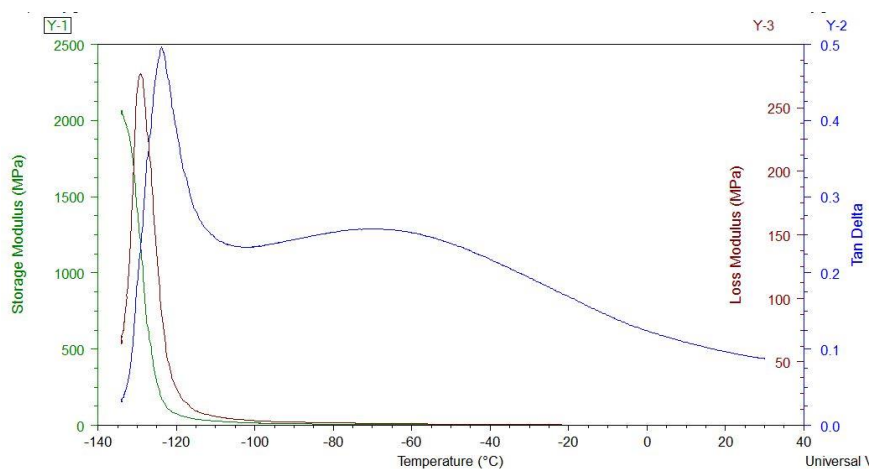


Figure 22. Storage modulus, loss modulus and tan delta as a function of temperature for Sylgard cured at 25°C.

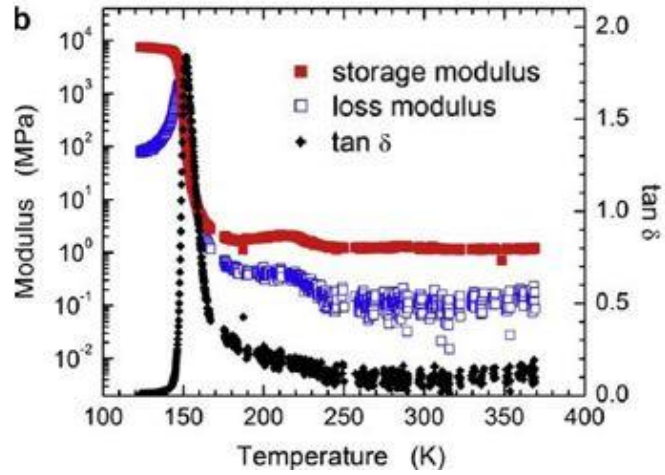


Figure 23. Storage modulus, loss modulus and tan delta as a function of temperature for Sylgard [41].

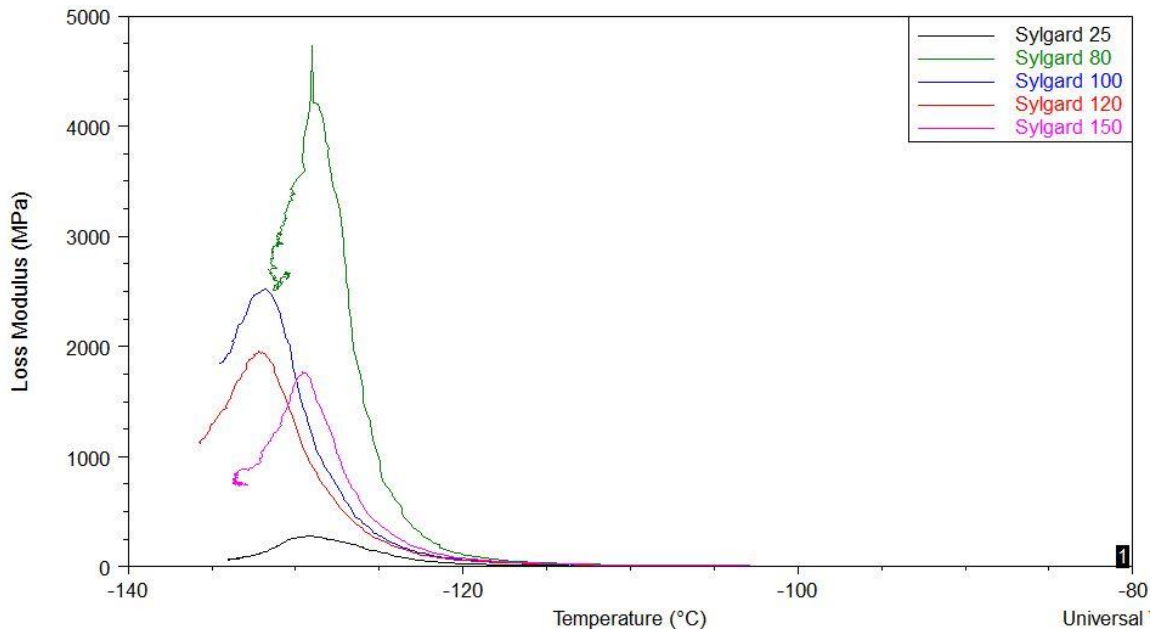


Figure 24. Loss modulus as a function of temperature of Sylgard samples cured at different temperatures.

Storage modulus is a measure of the stored energy, representing the elastic portion of the material as it undergoes relaxation. Therefore, it should decrease with temperature for polymer relaxation. Storage modulus for Sylgard peaks at around 100,000MPa at -143.14°C [41]. The machine that was used to run the DMA experiment was incapable of reaching that low of a temperature. Loss modulus is a measure of the energy dissipated as heat, representing the viscous portion. According to literature, typical values for Sylgard range from 1000MPa to 3000MPa. This matches closely to the plots in Figure 24.

Lastly, tan delta for all the Sylgard samples were plotted in Figure 25 below. The glass transition temperature (corresponding to tan delta peak) was found to be around -125°C. A table was compiled with the tan delta values of all the Sylgard samples.

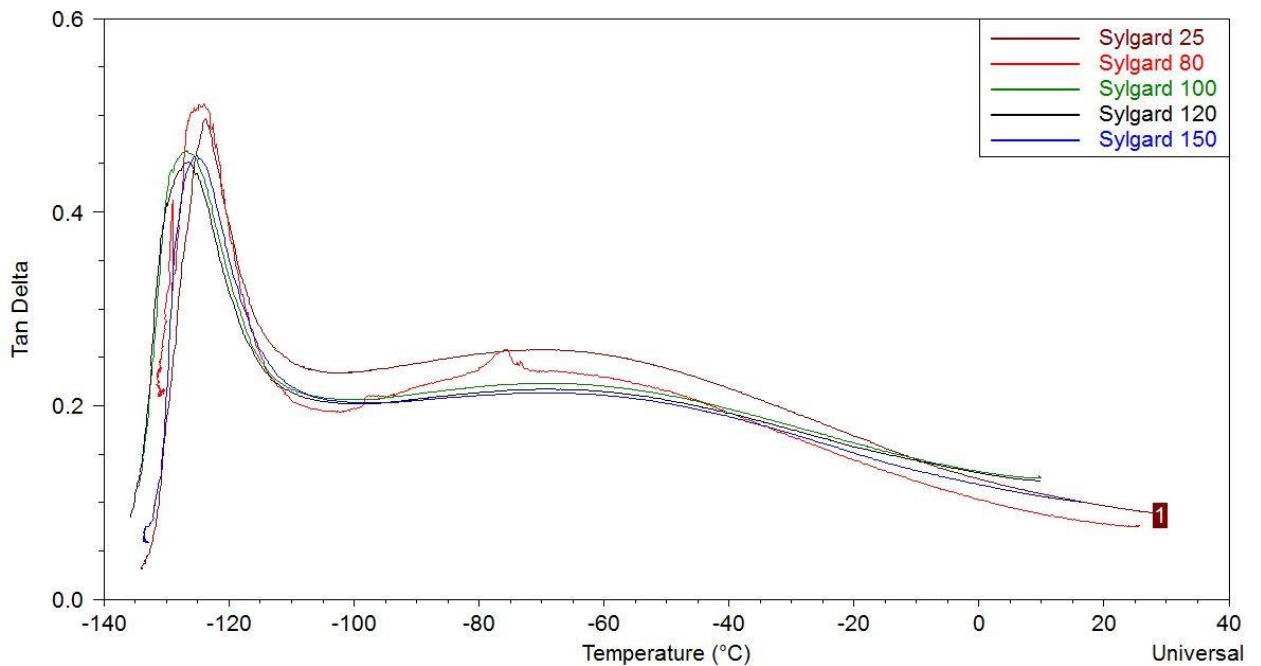


Figure 25. Tan delta for Sylgard samples cured at different temperatures.

Literature shows that the glass temperature of PDMS is -120°C [40]. However, from Table 4 below, the glass transition temperature is around -125°C . This is the temperature region where PDMS transitions from a hard, glassy material to a soft, rubbery material.

Table 4. Glass transition temperatures for Sylgard samples taken from tan delta peaks.

Sample	Temp. ($^{\circ}\text{C}$)
Sylgard 25	-123.74
Sylgard 80	-123.36
Sylgard 100	-125.98
Sylgard 120	-126.59
Sylgard 150	-125.31

The second peak at about -50°C , according to the manufacturer, is not a secondary transition for a termination molecule, but attributed to a structural relaxation [40].

4.2 Thermogravimetric Analysis

The Gelest and Sylgard samples were tested on the TGA machine shown in Figure 15. The samples weighed approx. 100gm were tested and their scans are presented in Figure 26 and Figure 29 below. The analysis was run from room temperature to 800°C at a rate of 5°C per minute.

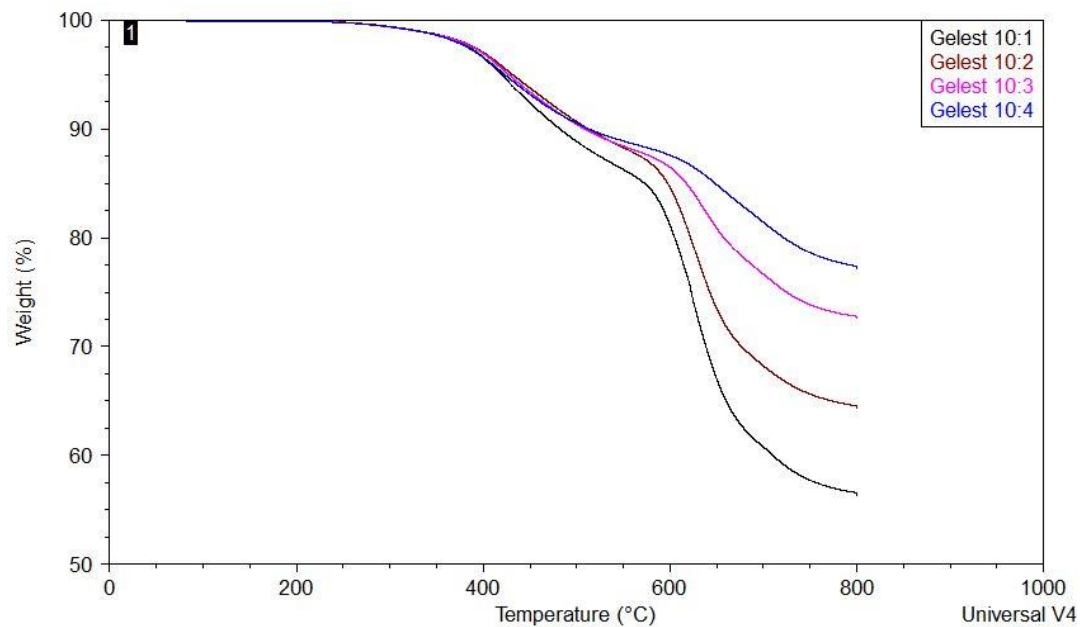


Figure 26. Weight loss as a function of temperature for Gelest samples.

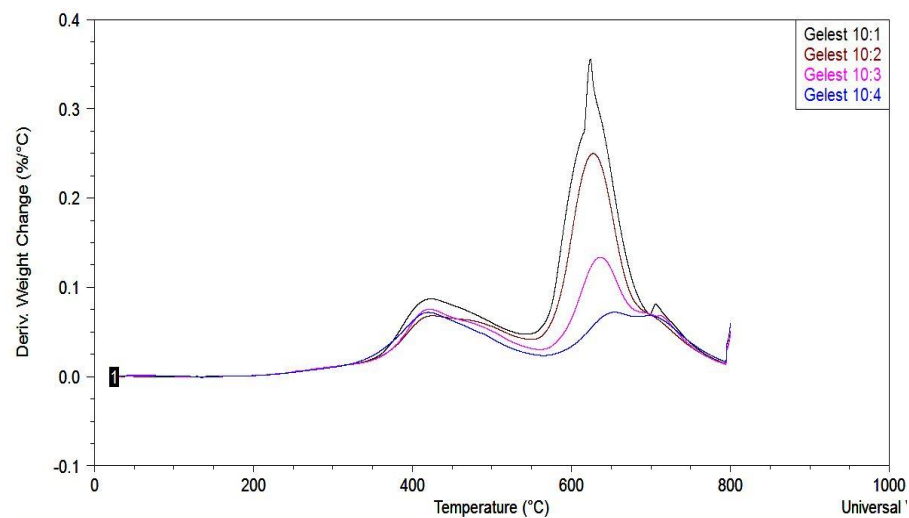


Figure 27. Differential weight change as a function of temperature for Gelest samples.

Gelest experienced a two stage degradation as depicted in Figure 27. The first decomposition temperature was around 450°C and the second decomposition temperature was around 650°C. There is no report on literature which suggests that

parts (bonds) decompose at two different stages yet. However, there exists a relationship between bonding intensity and the decomposition, i.e. a strong bond has a corresponding higher decomposition temperature, while a weak bond has a lower decomposition temperature. Typical bond energies of C–C, C–O, C–H, and Si–Si are 349, 370, 337, and 327 kJ/mol respectively [43]. The single bonds of C–C, C–O, C–H, and Si–Si are susceptible to chain scission during thermal degradation and act as weak links, which correspond to the decomposition of Gelest during the first stage. The second decomposition, characterized by the second peak can be [42,43] attributed to the degradation of Si–O bond, where the Si–O bond energy is 798 kJ/mol.

Figure 28 illustrates a clear increase in residual mass with decreasing silica content. This is better represented in Figure 28 below. There was an increase in residual mass with an increase in silica. Silica is not as easily decomposable as the other compounds in Gelest, therefore the more silica was added the more the mass remained after decomposition.

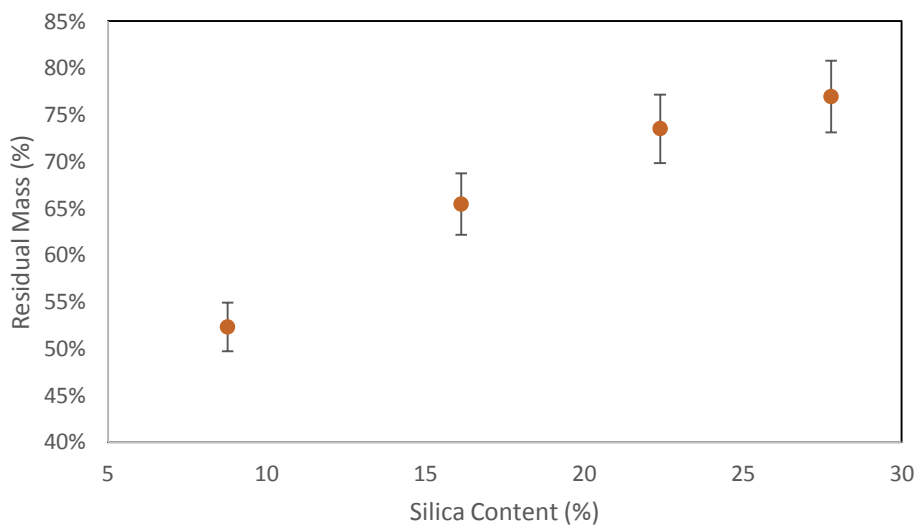


Figure 28. Residual mass as a function of silica content after TGA test for all Gelest samples.

The Sylgard samples in Figure 29 do not show a clear trend in the residual mass left after the thermogravimetric analysis on the samples cured at different temperatures.

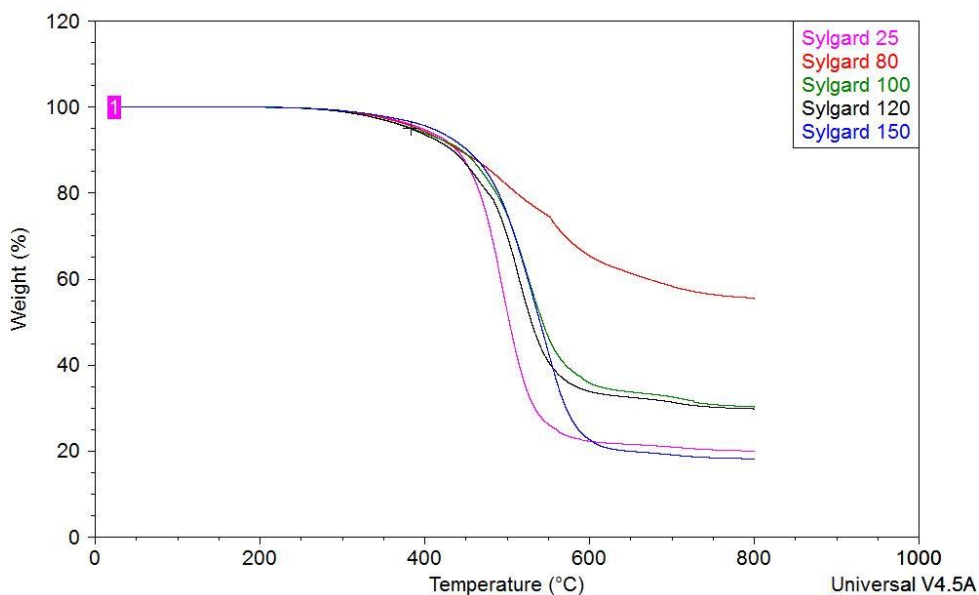


Figure 29. Weight loss as a function of temperature for Sylgard samples.

In Figure 30, Sylgard underwent one stage degradation due to the decomposition from 400°C to 600°C of the weak bonds as earlier discussed.

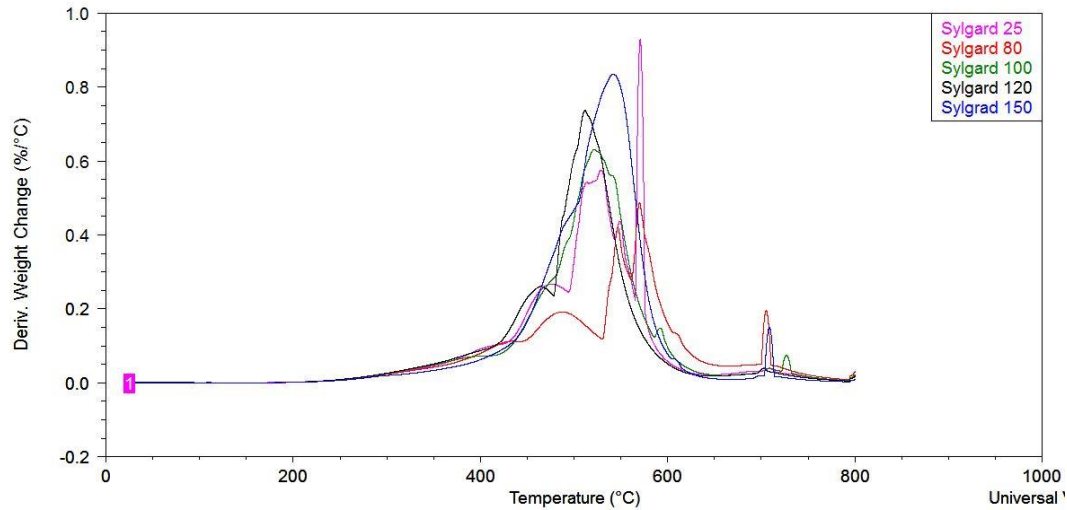


Figure 30. Differential weight change as a function of temperature for Sylgard samples.

The sample Gelest 10:1 containing 9% silica lost almost half of its mass after 800°C while Gelest 10:4 that contained 30% silica retained 70% of its mass after 800°C. A 1% increase in residual mass after 800°C requires ~1.19% increase in silica content in the Gelest™ samples.

4.3 Finite Element Analysis

The tension test was simulated in ANSYS™ Workbench. Since the sample was only pulled in tension up to 10% strain, a linear model was used. The material properties used for simulation were 1.84 MPa for the young's modulus and 0.45 for the Poisson's ratio [44, 45]. A zero displacement was placed on the bottom surface and a 6.5 mm displacement placed on top of the sample to simulate the 10% strain as shown in Figure 31 below.

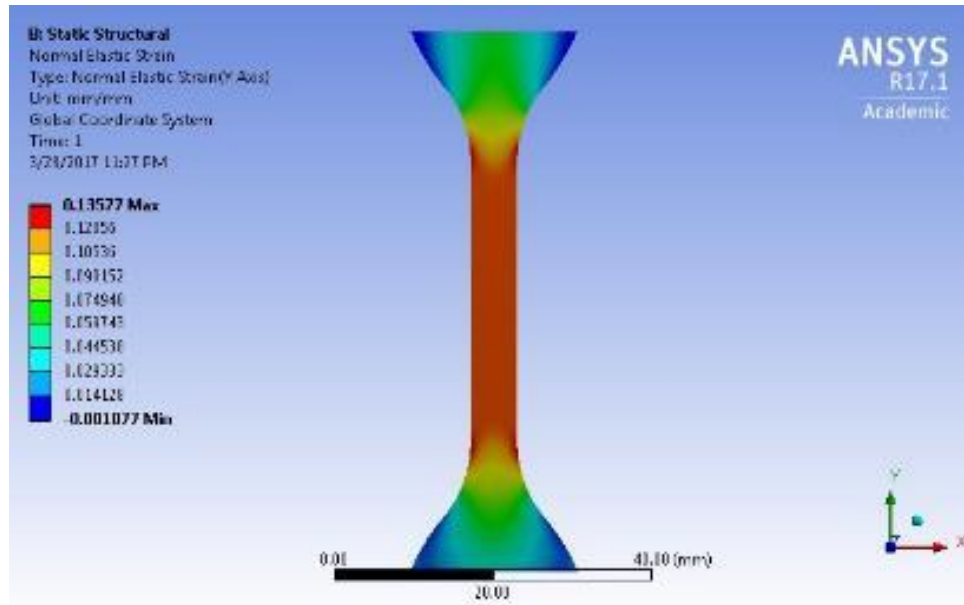


Figure 31. Finite Element Analysis at 10% strain showing uniform strain on the gage section.

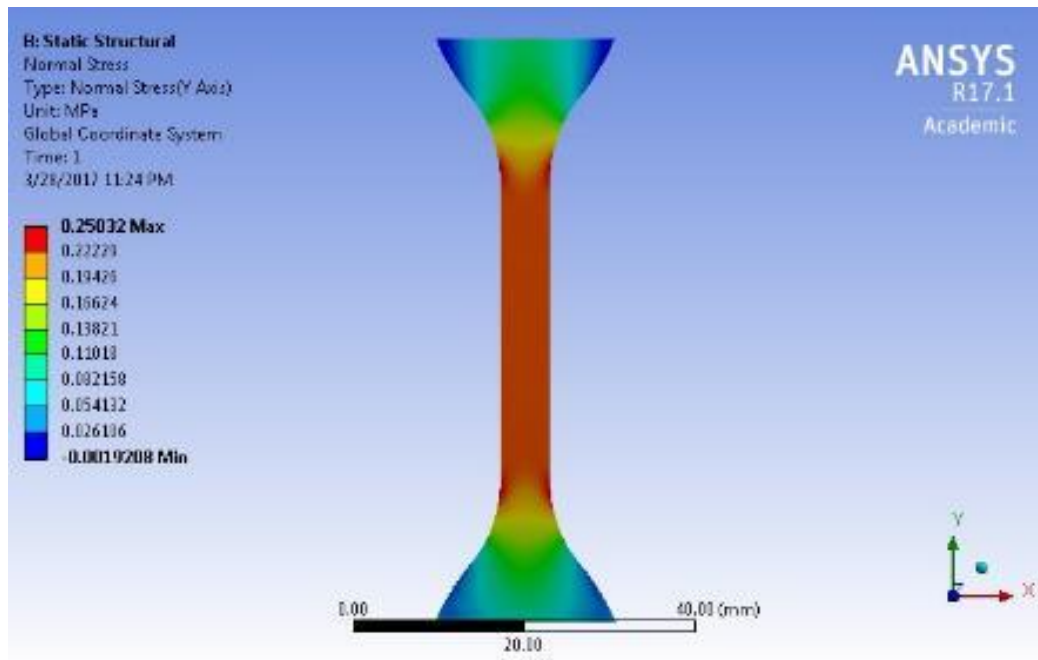


Figure 32. Finite Element Analysis at 10% strain showing uniform stress on the gage section.

The FEM analysis proves that the strain distribution is only uniform in the gage section. To record accurate values for strain, we only need to capture the strain data from this section. Since the material being tested is highly flexible, a non-contact method is the best option. This analysis also shows that the strain captured by the crosshead is inclusive of the strain that is perturbed by the change in geometry. This will lead to erroneous calculations of the material properties such as young's modulus.

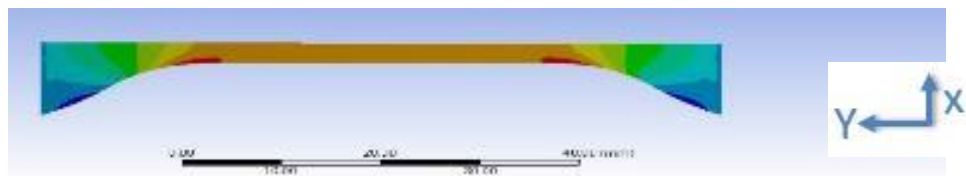


Figure 33. Cross-section of Finite Element Analysis at 10%.

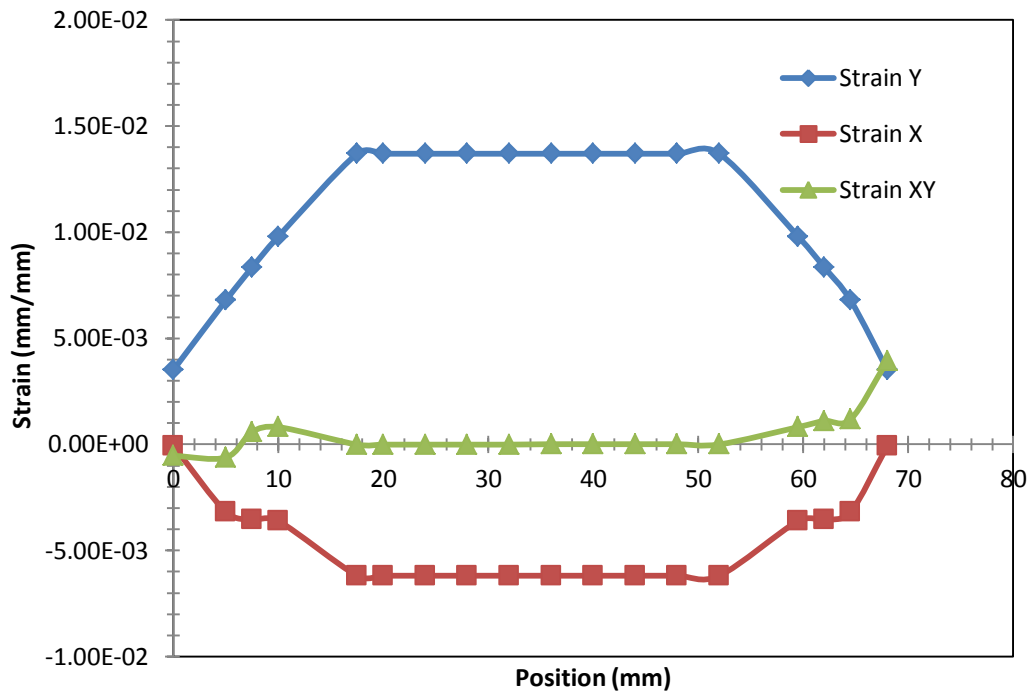


Figure 34. Strain as a function of position from cross-section FEA.

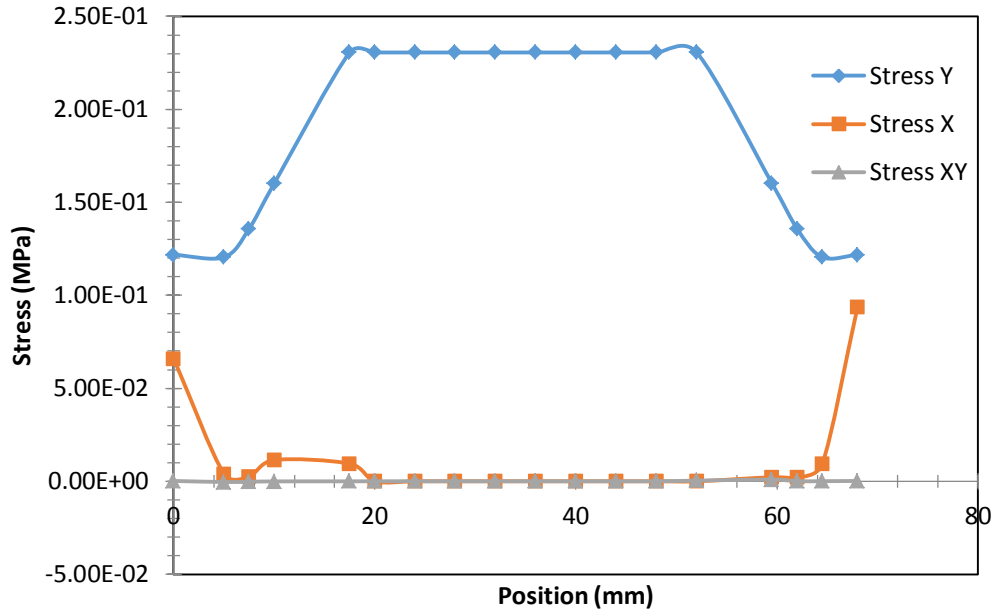


Figure 35. Stress as a function of position from cross-section FEA.

Figure 34 supports that the PDMS sample in tension experiences negligible shear strain while the strain in the y-direction is ~ 2.28 times the strain in the x-direction corresponding to a Poisson ratio of 0.45 which was used in the analysis. Figure 35 shows that there is no shear stress and more importantly the only stress in the x-direction is found in the non-gage section area. A majority of the stress is taken up by the gage section hence the use of the gage section dimensions as inputs when running a tension test on the Instron™ machine.

$$\sigma_x = \frac{E}{1-\nu^2} (\epsilon_x + \nu\epsilon_y) \quad (15)$$

Equation 15 is from 2D Hook's law. It is used to explain why the strain in the x-direction in Figure 34 does not translate to stress in the x-direction in Figure 35. Deformation is only in the y-direction, hence the strain and stress values present in both graphs in that direction. Strain in the x-direction is due to Poisson's ratio effects which

dictate that the sample will get thinner in the gage section with displacement in the y-direction. This can be proved using 2D Hooke's law that can map the strain values along the gage section. The presence of stress in the x-direction at the 0mm position and the 65mm position is because of boundary condition effects. The constrains at the ends subjects the material to stresses that can accurately mimic what the grips on the Instron machine would have on the sample being tested.

4.4 Mechanical Characteristic Analysis of PDMS in Tension

When it comes to strain measurement of hyper-elastic materials, it is essential to capture the true displacement. A sample was tested and data from the non-contact measurement (video extensimeter) and from cross head were plotted below.

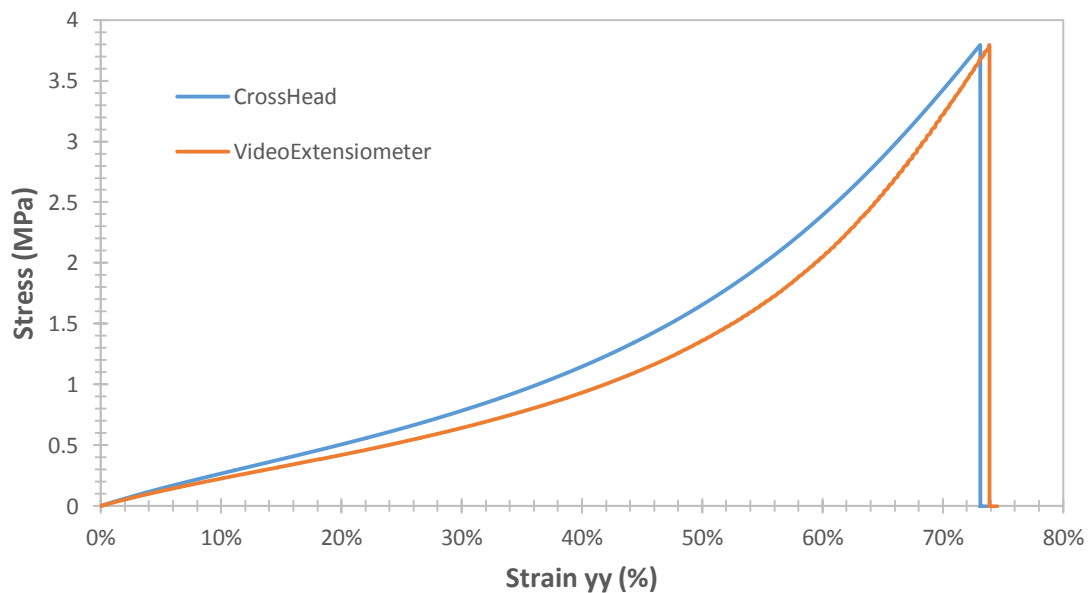


Figure 36. Stress-strain relationship of different strain measurement techniques.

Figure 36 above shows a clear difference in strain obtained from the crosshead and the video extensometer. This inaccuracy has been included in numerous reported

values for the mechanical characteristics of PDMS. In order to correct the crosshead strain measurement, we will have to break down the strain contribution from the different geometries. Young's modulus was 2.21MPa from crosshead reading and 2.03MPa from video extensometer. The difference comes Figure 37 below gives a breakdown of the regions in a tension sample.

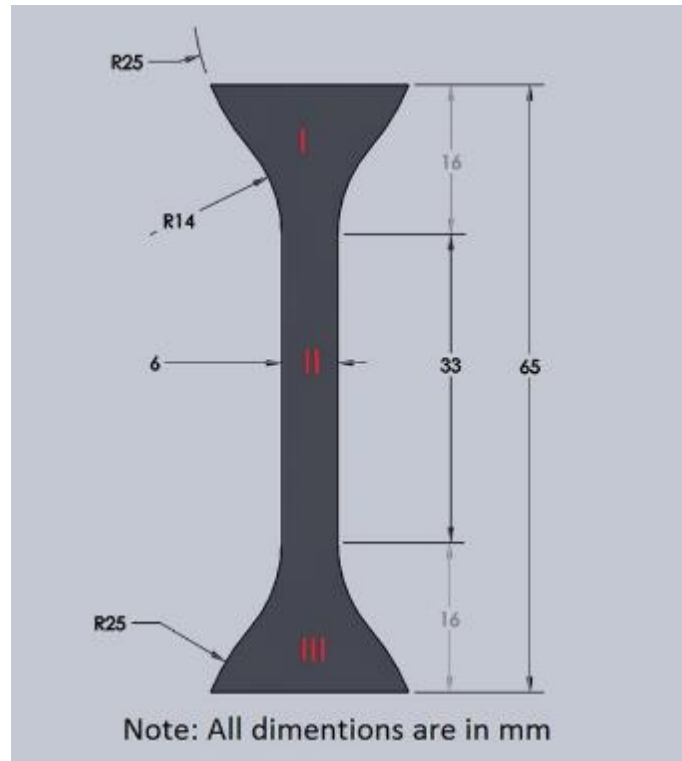


Figure 37. Exposed strain regions of PDMS sample.

The crosshead incorporates strain from region I, II and III while the video extensometer only includes strain from region II. We assume that the entire sample experiences the same load, the strain measurement in region I and II are identical and that the total extension of the sample under tension includes the extension from region I, II and III. In order to find the correction factor, we need to calculate the difference in

magnitude of the strain experienced by the entire sample (region I,II and III) to the strain experienced by the gage section (region II). For this, equation 15 holds true.

$$\Delta^T = 2\Delta' + \Delta'' \quad (15)$$

Where Δ^T is the extension that the entire sample experiences under tension, Δ' is the extension by region I and Δ'' is the extension by region II. At a given load the entire sample experiences a certain displacement Δ^T . With the area and lengths of the different regions known, solving for Δ' and Δ'' is possible. The strain for region II was calculated by dividing the extension of the region (Δ'') by the length of the region II (33mm). The extension (Δ'') was obtained from the video extensometer reading. This resulting strain was compared to the strain given by the crosshead ($\Delta^T/65mm$) for every loading condition from 0-10% strain. The average of the factor (ϵ''/ϵ^T) was found to be 1.198. This means that the gage section experiences 20% more strain than what the crosshead records. Multiplying the strain from the crosshead with the factor of 1.198 matches the strain from the video extensometer thereby confirming our deduction.

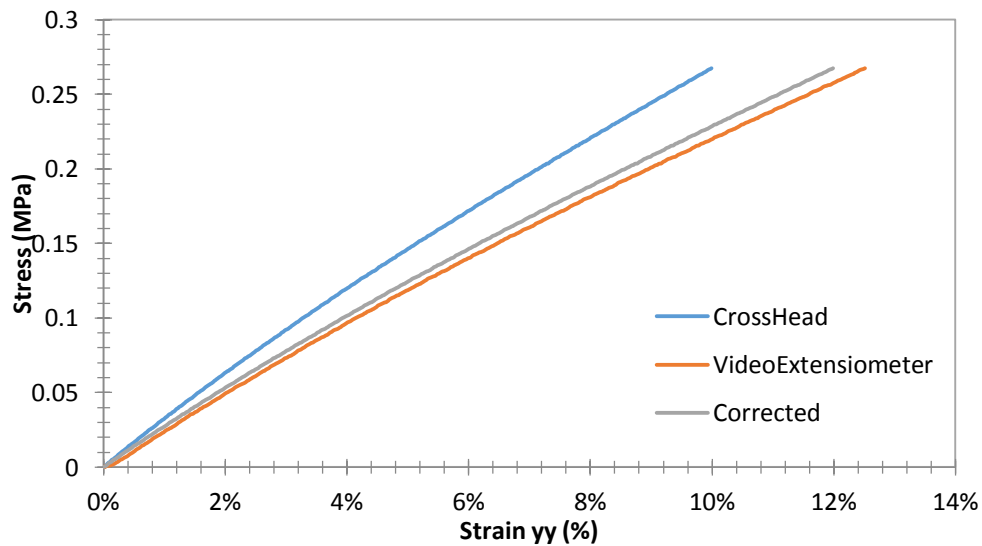


Figure 38. Corrected crosshead strain of Sylgard sample cured at 25°C.

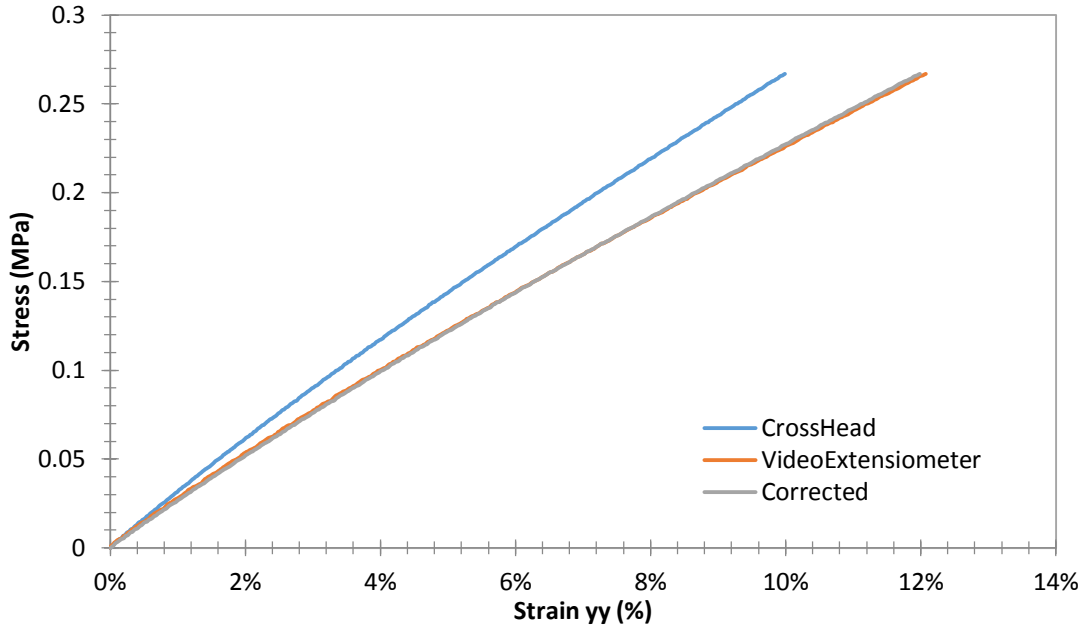


Figure 39. Corrected crosshead strain of Sylgard sample cured at 80°C.

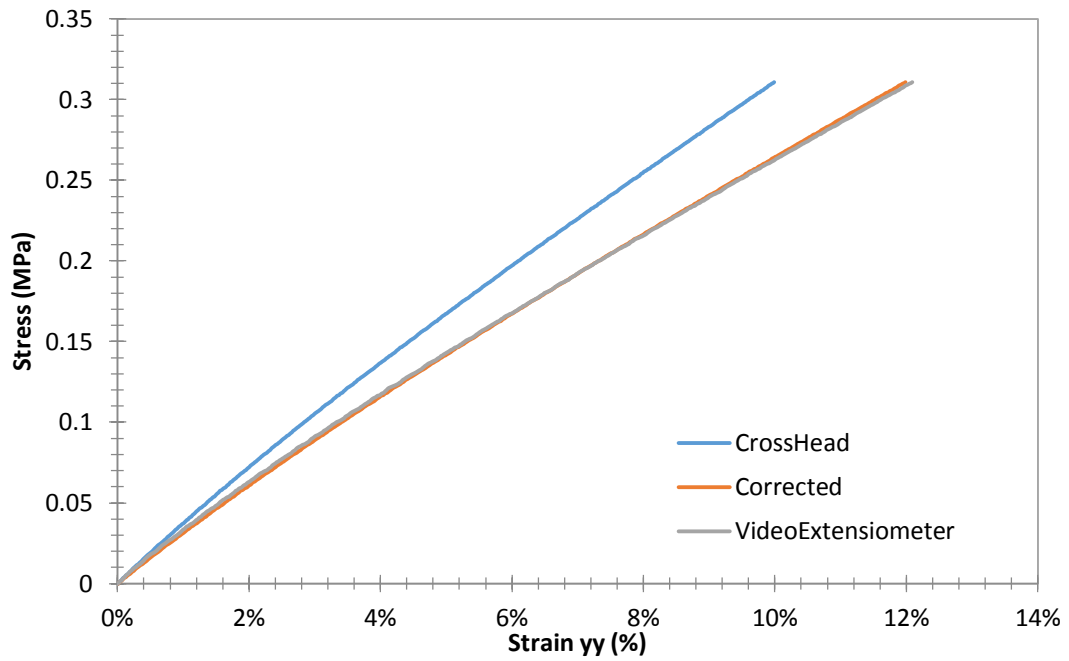


Figure 40. Corrected crosshead strain of Sylgard sample cured at 120°C.

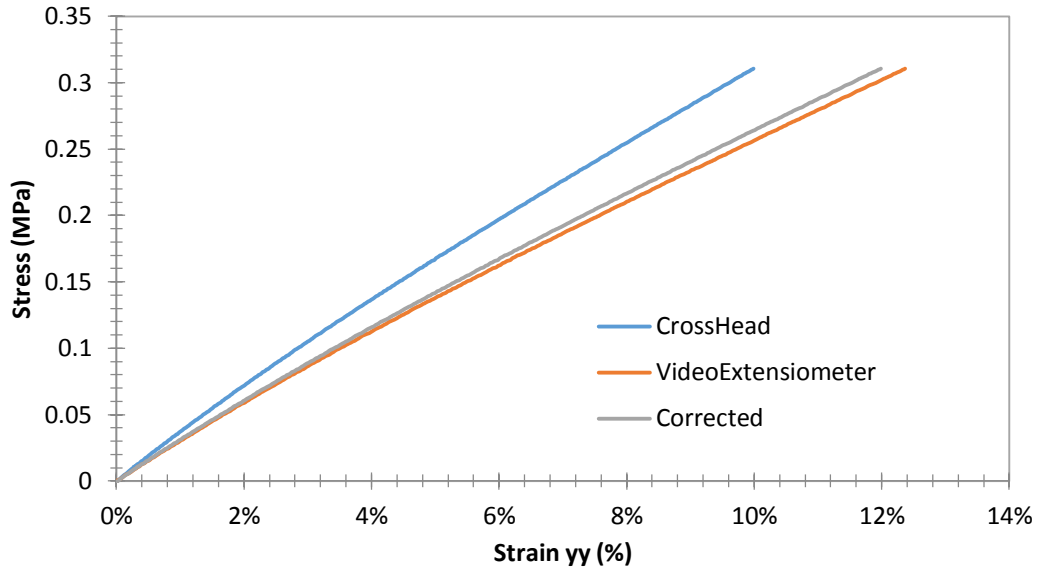


Figure 41. Corrected crosshead strain of Sylgard sample cured at 150°C.

Figure 38 through to Figure 41 show the correction factor aligning the crosshead strain of Sylgard™ samples cured at different temperatures perfectly to the video extensometer strain plot. This proves that the correction factor is not affected by the cure temperature of the samples.

There is a distinct difference between the two slopes from the DIC and the crosshead plots in Figure 42 below. The DIC slope is more accurate because only the gage section region is correlated while the crosshead incorporates the strain of the entire sample, inclusive of the areas of non-uniform strain. This leads to misrepresentation of a basic stress-strain plot which in turn leads to inaccurate values for the young's modulus. DIC techniques gives a modulus of 1.8MPa while the crosshead gives a modulus of 2.07MPa, 15% more than the latter. This is significant difference to be overlooked when it comes to characterizing a material for a specific utility.

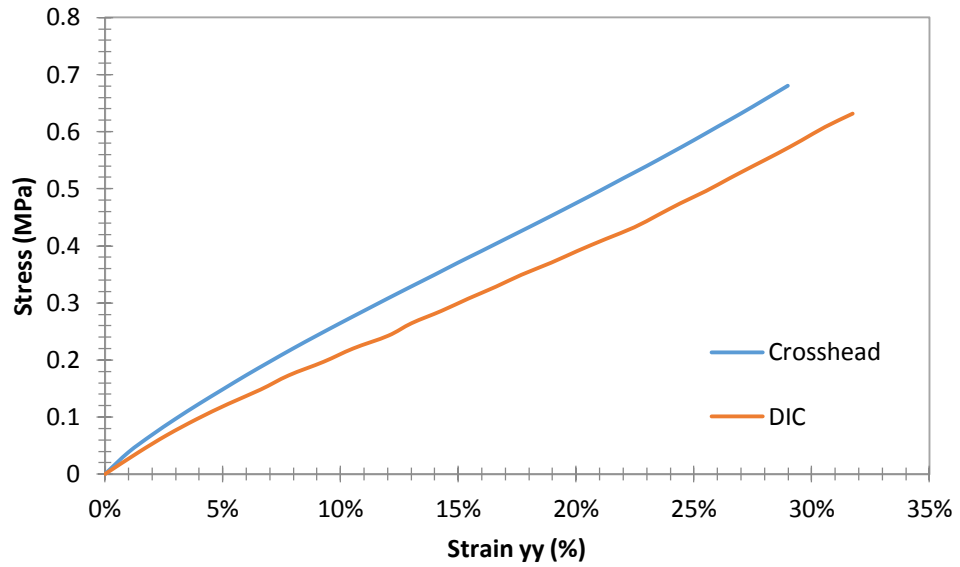


Figure 42. Comparison of stress-strain relationships between crosshead and DIC data.

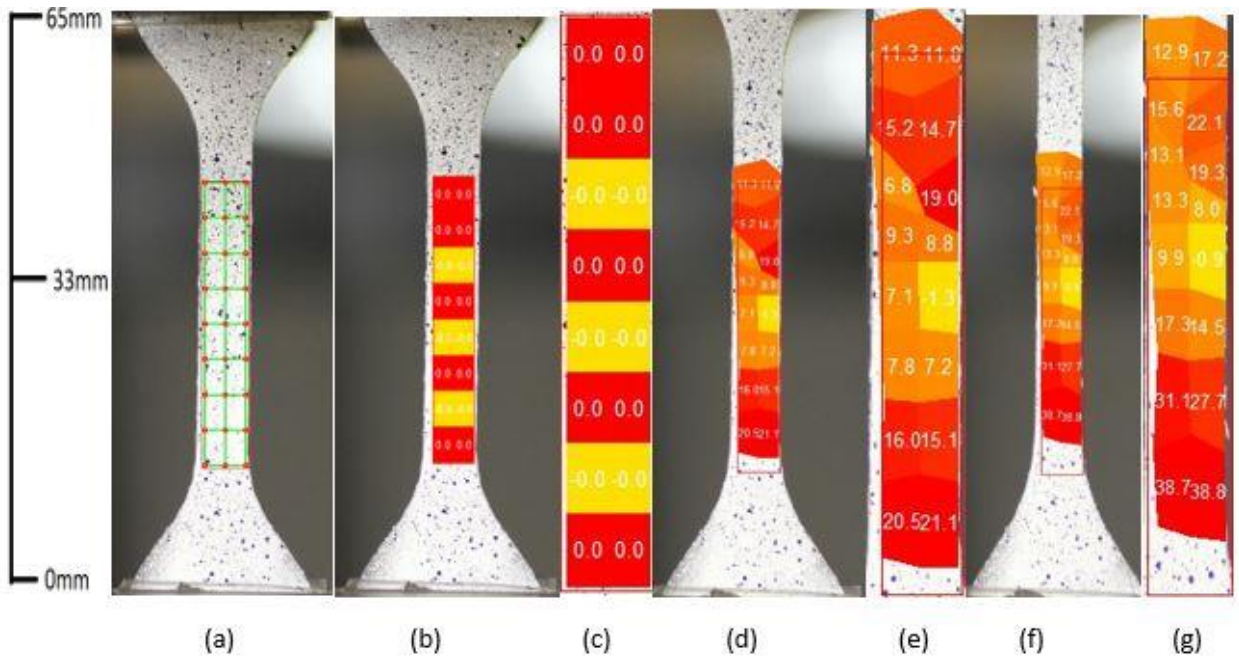


Figure 43. Strain field of PDMS in tension.

Figure 43 illustrates the strain field at different strain levels in the direction of displacement. Image (a) shows the region of interest from which 16 subsets were created

to correlate the corresponding strain patterns. Image (b) shows the strain field right before the tests starts. Image (c) is an expansion of the region of interest in Image (b). Image (d) shows the strain field at the middle of the experiment, an average of 15% strain. Image (e) is a focus of the strain field in Image (d). In Image (e), the strain values are decreasing moving upwards, this is simply because the sample is fixed at the bottom and the direction of the pull is upwards. Image (f) was the last image of the experiment with an average value of 32%. Image (g) is an expansion of Image (f). The more the sunsets, the more accurate the strain values since the correlation is calculated from multiple points in the subset.

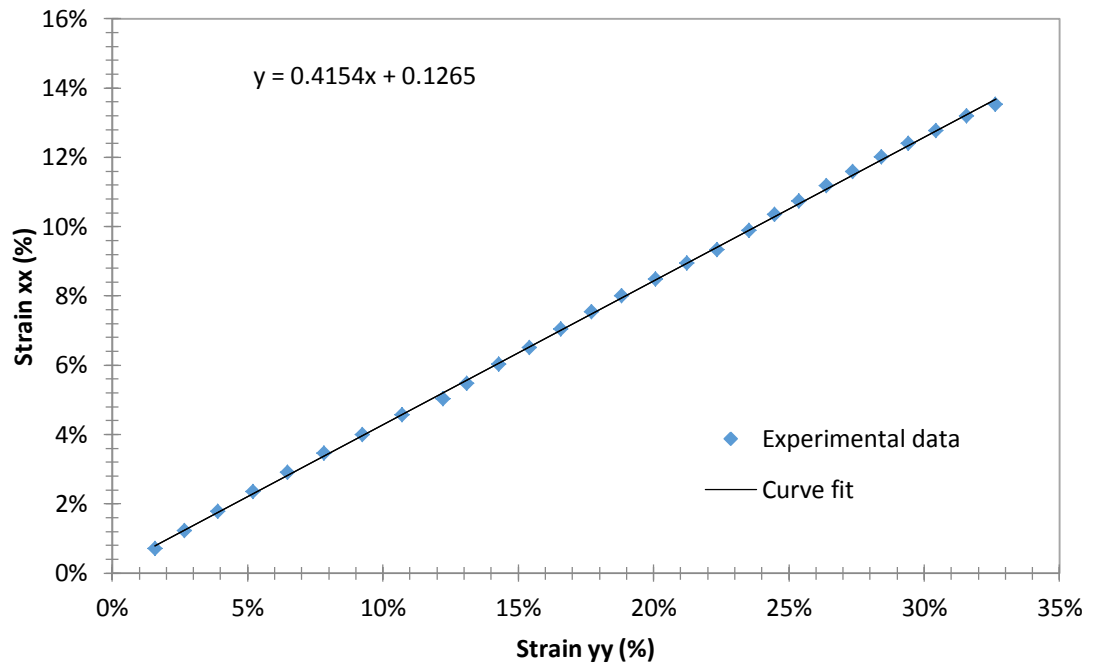


Figure 44. Slope of strain in x and y direction.

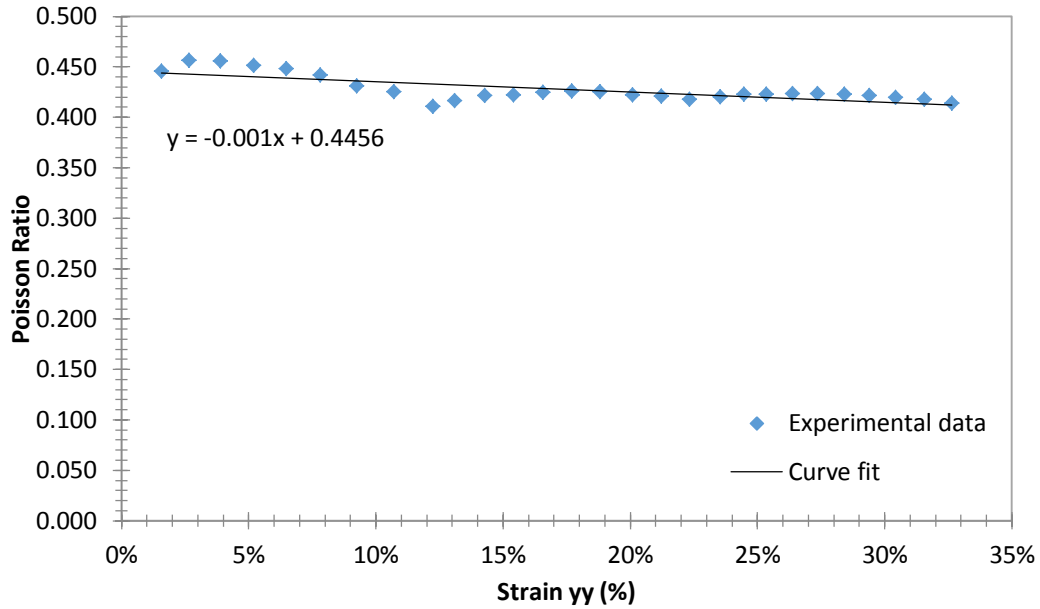


Figure 45. Poisson ratio as a function of strain in the y direction.

From Figure 44, a linear regression analysis lead to a Poisson ratio of 0.4147, this is different from the value of 0.45 that is widely used for Sylgard® 184 in literature and FEM Analysis[40]. Figure 45 reveals that the Poisson ratio decreases with increasing strain, this means that the sample is stretching in the Y-direction much faster than it is contracting in the X-direction. This is supported when it is visible that the gage section is undergoing necking, the gage section becomes thinner, during the tension test. This data also shows the discrepancy that is involved in modeling a tension test of a hyperplastic material such as PDMS with a constant Poisson ratio.

Theoretically, in a uniaxial test, there is no shear strain since the material is only subjected to displacement in one direction. The presence of shear strain proves that either the sample was not perfectly aligned with the camera or it was not secured perfectly parallel to the Instron machine grips. The shear strain was minimal, 0.5 % shear strain to

30% strain in the y-direction. This error is acceptable given that the sample was secured manually and the camera was set using a spirit level.

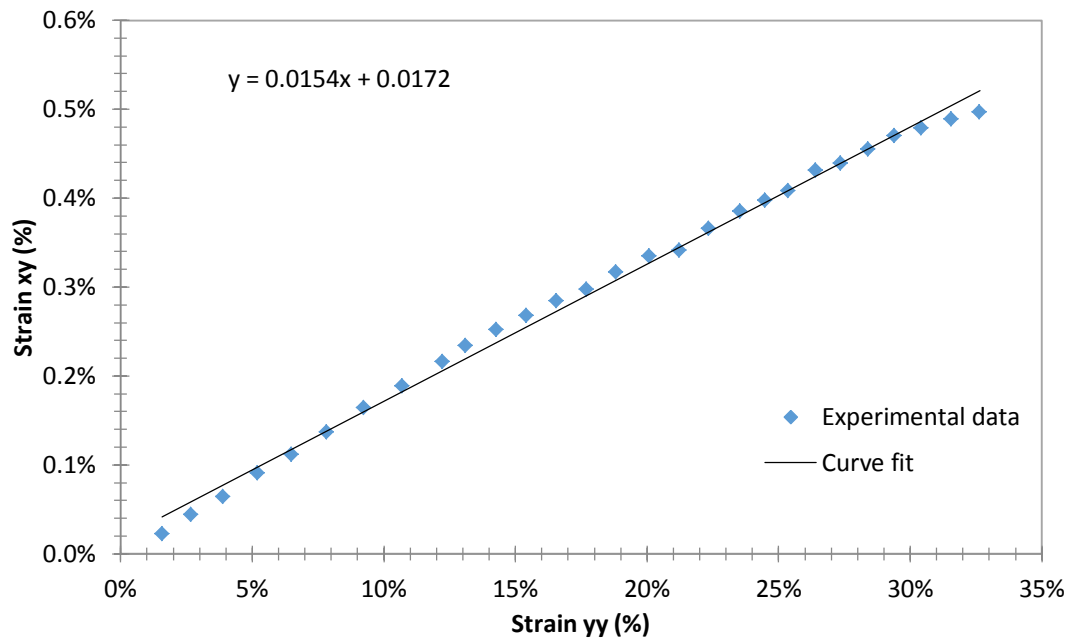


Figure 46. Shear strain as a function of strain in the y direction.

Local strain patterns were studied half way along the region of interest. Figure 47 shows the line scan denoted by a black line.

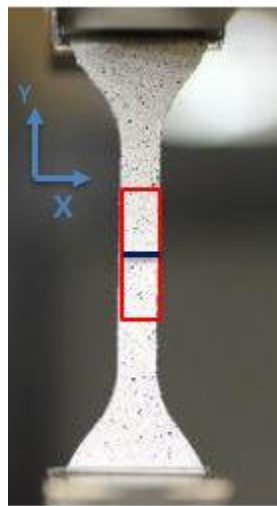


Figure 47. Line scan half-way from top of region of interest (ROI).

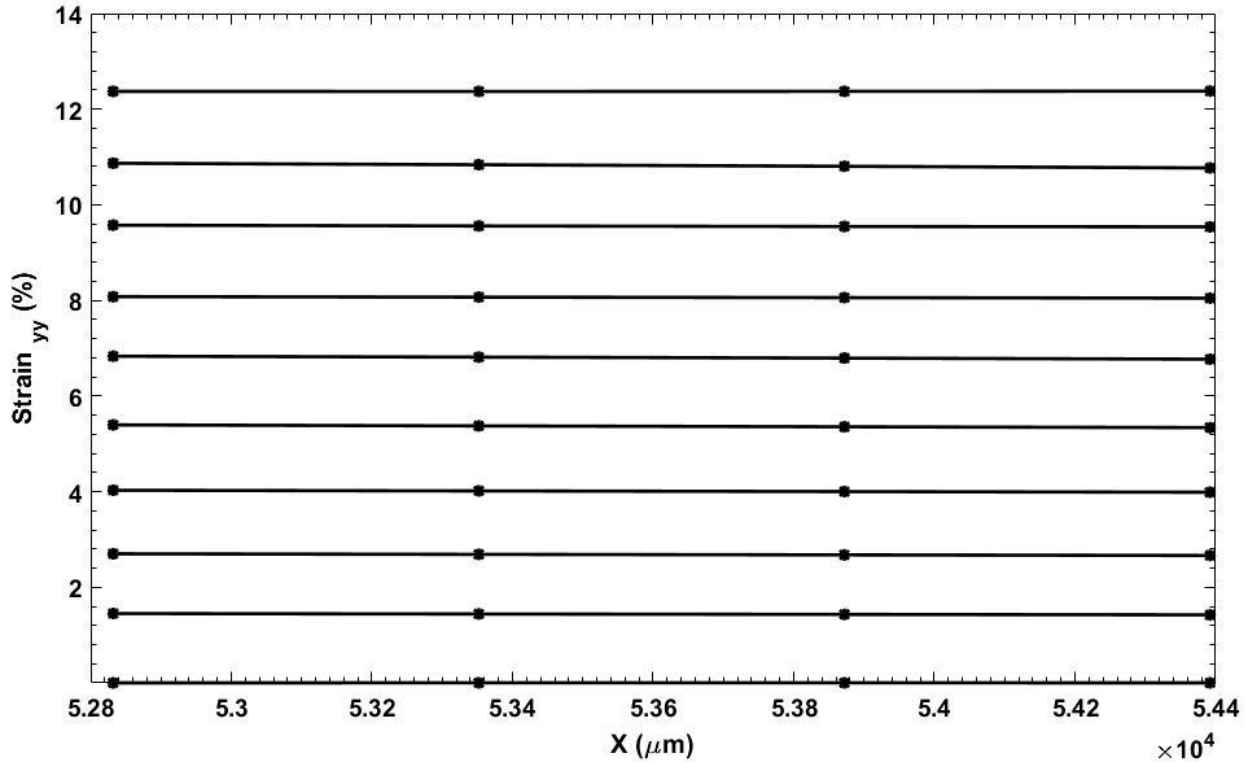


Figure 48. Strain in y-direction along the horizontal line half-way from top of ROI.

In Figure 48, line scans of the Sylgard™ tension sample were taken 0.5 from the region of interest which is located in the middle part of the gage section where the strain pattern is uniform. The x-axis is the length of the ROI and the y-axis is the strain corresponding to the different line scans. Each line scan corresponds to one image, a total of 10 line scans, 10 images covering strain from 0 – 12.24% in the y-direction. This figure shows how uniform the local strain is at the middle of the sample.

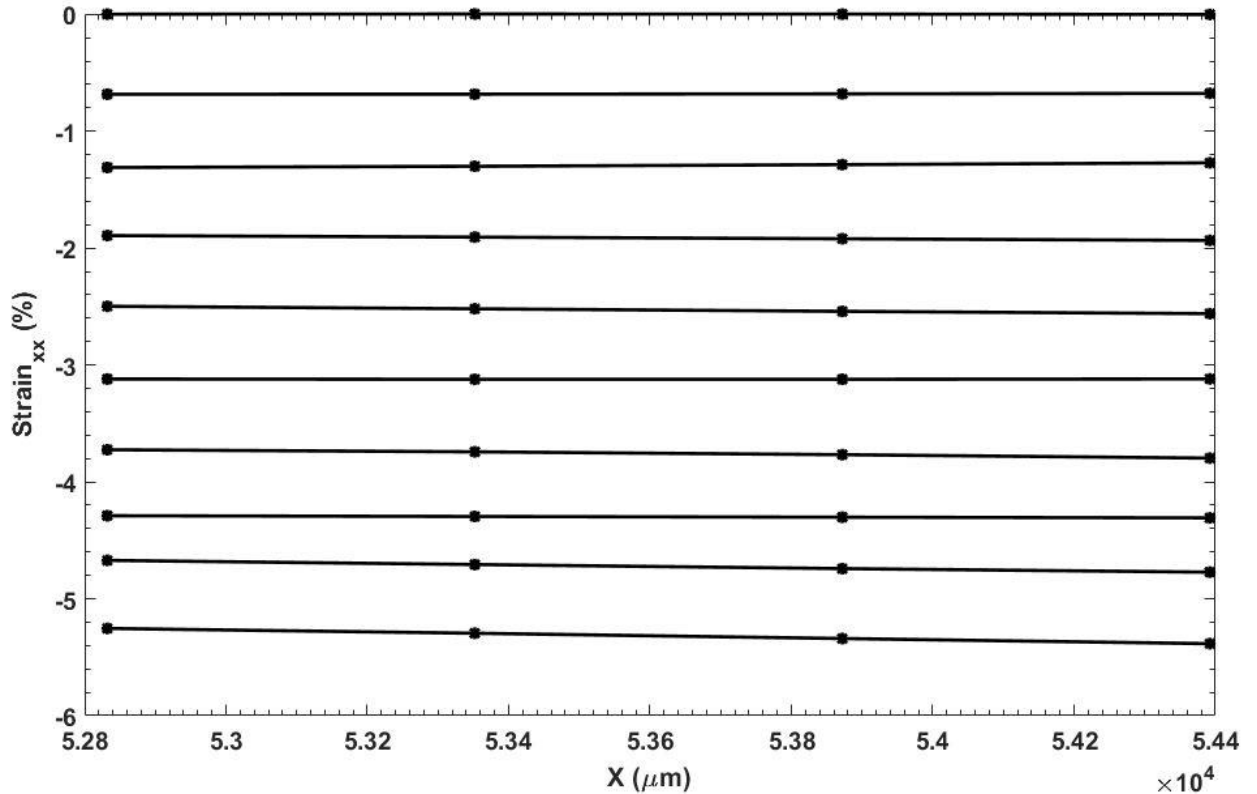


Figure 49. Strain in x-direction along the horizontal line half-way from top of ROI.

Similarly, Figure 49 represents line scans of the Sylgard™ tension sample were taken 0.5 from the region of interest which is located in the middle part of the gage section where the strain pattern is uniform. The line scans show a uniform pattern in strain in the x-direction as the sample experienced a global strain from 0-12.24% represented by the 10 line scans in the figure.

This information, made only available through DIC is able to give researchers an in depth view of how the local strain compares to the global strain. This can be useful in manufacturing PDMS polymers of different geometries for microelectromechanical systems because the strain patterns can be analyzed on a local level and leading to the

production of optimized geometries with well understood deformation patterns under specific loading conditions.

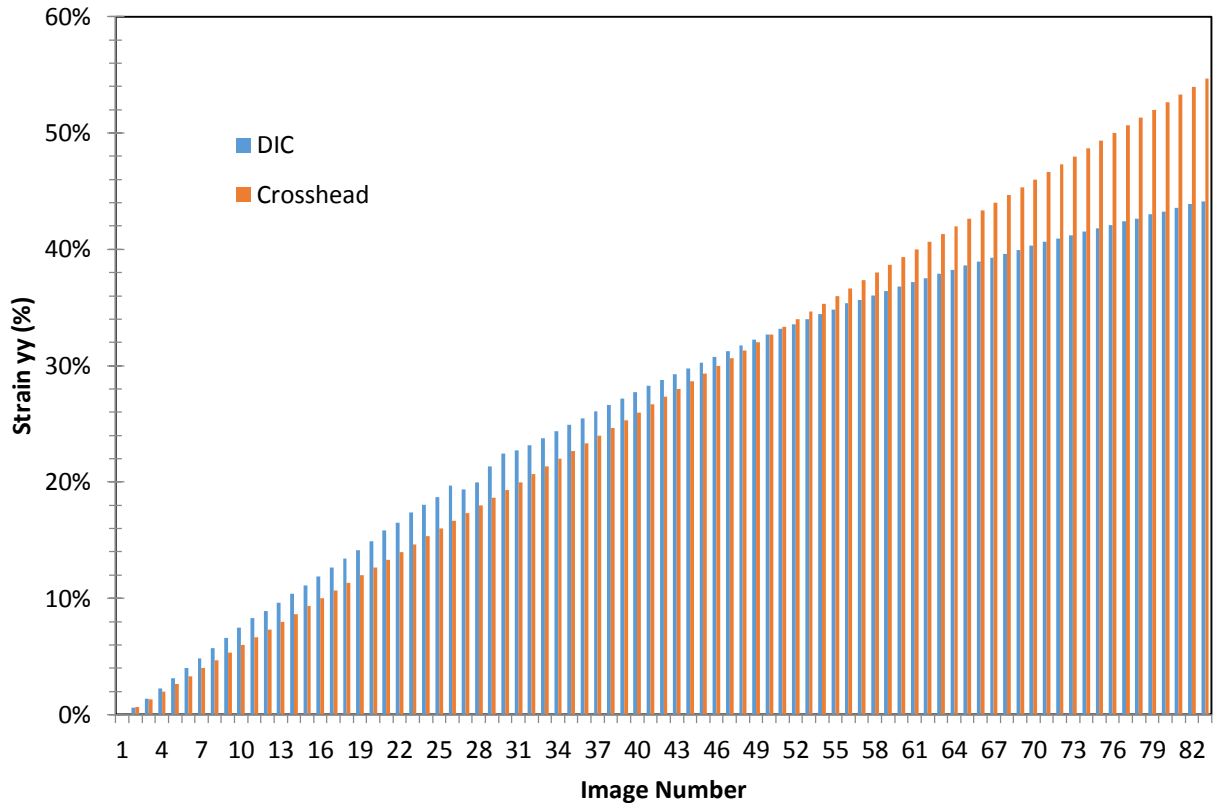


Figure 50. Strain profile for DIC and Crosshead techniques.

Figure 50 shows a progressing difference in the strain measurements from DIC and Instron. The crosshead data from the Instron machine is linear, absent of the non-linearity associated with hyper-elastic materials. This goes to prove that DIC is more accurate in mirroring hyper-elastic materials in tension.

4.5 Mechanical Characteristic of PDMS in Compression

The compression test carried out on the 10mm cube PDMS sample was done with a strain rate of 20% per minute which translates to 2mm per minute. An image was taken

after every 5 seconds. The data was compiled and analyzed in MS Excel and the following plots were developed.

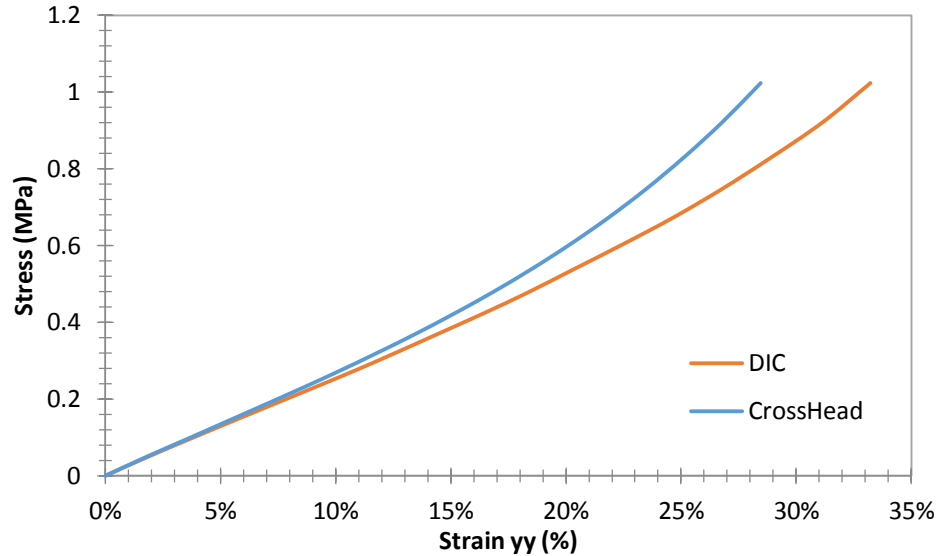


Figure 51. Stress-strain relationship between DIC and Crosshead compression test data.

From the compression tests, the modulus from the two plots were obtained from the 0-10% strain range. The compressive modulus was 26.7MPa and 25.2MPa for the Instron and DIC respectively with a difference of 6%. DIC is taken to be more accurate than the Instron reading because DIC only calculates the strain of the region in the middle of the sample unperturbed by the boundary between the sample and the machine platen as can be seen in Figure 52.

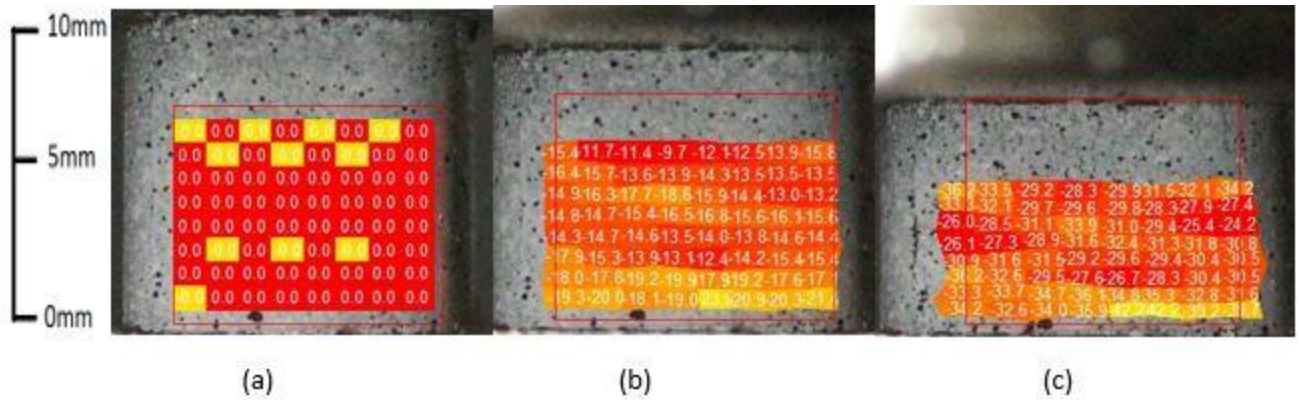


Figure 52. Strain field of PDMS in compression

Figure 52 illustrates three different strain fields for three different strain levels. Image (a) shows the strain field at the very start of the experiment before the test runs. The average strain value at this instance is 0%. Image (b) corresponds to an average of 15% and was taken at the middle of the experiment. Lastly, Image (c) was taken at the end of the experiment and it corresponds to an average of 31% strain. The strain values are increasing from top to bottom because that is the direction in which force is being applied. The progression of the images shows a decrease in height and an increase in width as a result of the sample being compressed.

The Instron machine takes the strain of the entire sample which includes that regions near the platen which experience non-uniform strain. This difference is not as significant between 0-10% given that the compressive modulus from both techniques only had a difference of 5%, however this difference increases significantly with increasing strain as can be inferred in Figure 51.

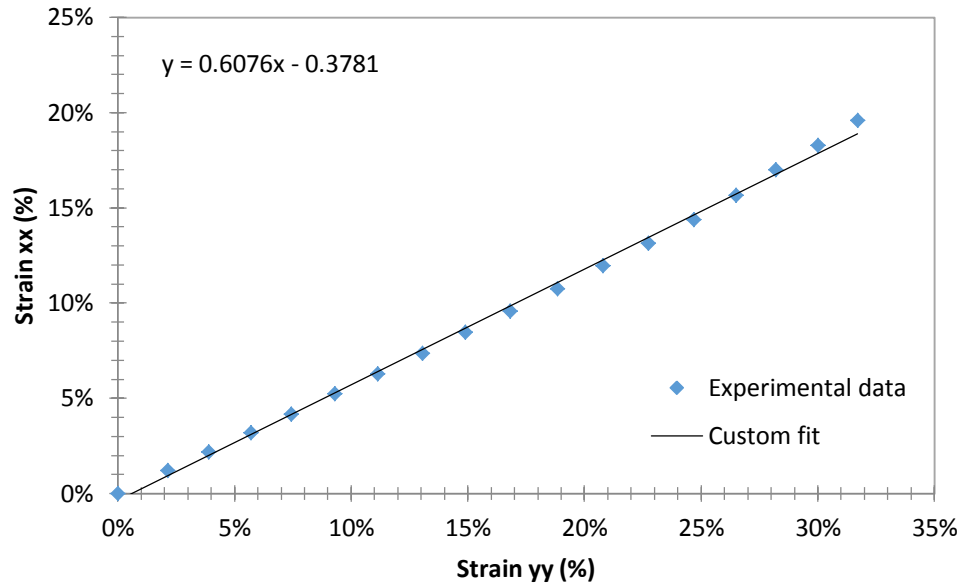


Figure 53. Slope of strain in x and y direction of compression Sylgard sample.

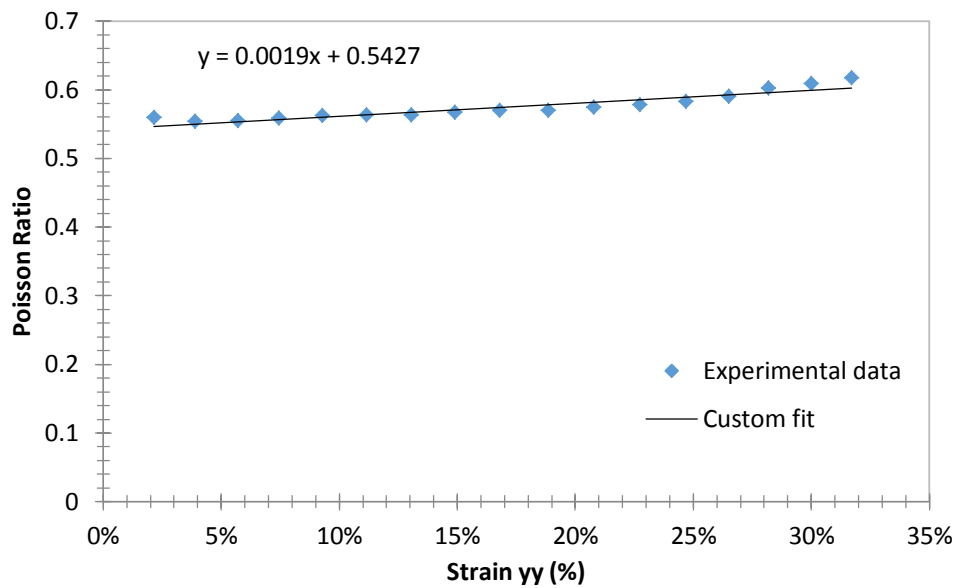


Figure 54. Poisson ratio change as a function of strain in y direction.

The Poisson ratio of the samples in compression are fairly linear with an average of 0.6067. It is important to note that it is higher than the Poisson ratio recorded for the tension samples. Figure 54 shows an increasing trend in the Poisson ratio with increasing

strain. This means that the sample was increasing in the transverse direction much faster than in the axial direction. We can also conclude that FEM Analysis in tension and compression require different Poisson ratios.

Similarly, to the tension samples, the compression samples experienced an unprecedented shear strain. Again, this low level amount of shear strain, 0.7% for 30% strain in the transverse direction, can be attributed to the manual setup of the sample onto the Instron machine or the slight misalignment of the camera to the sample surface.

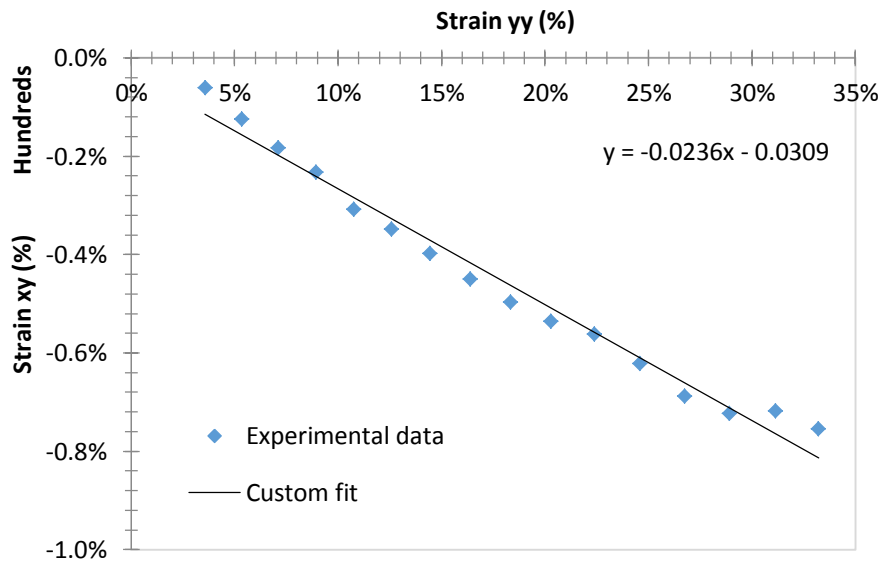


Figure 55. Shear strain as a function of strain in the y direction.

Local strain patterns were studied half way along the region of interest. Figure 56 shows the line scan denoted by a black line.

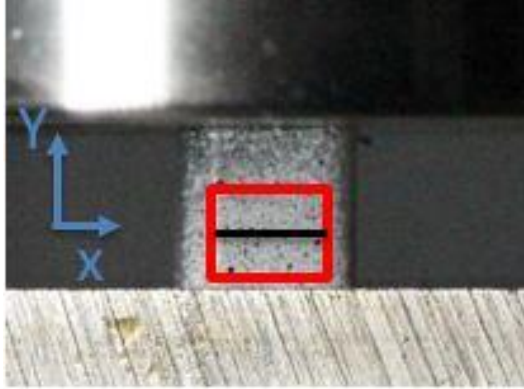


Figure 56. Line scan at half-way from top of region of interest (ROI).

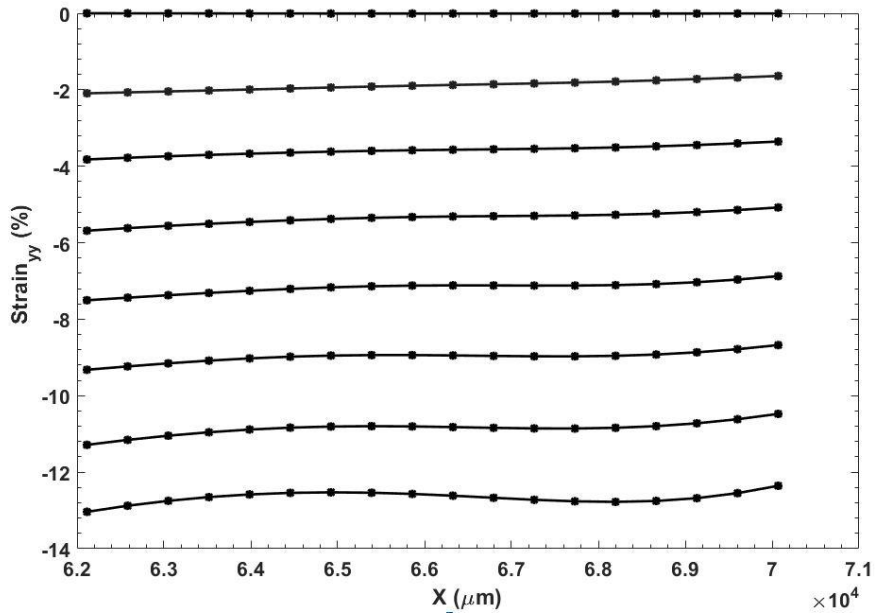


Figure 57. Strain in y-direction along the horizontal line half-way from top of ROI.

Figure 57 shows the uniformity in strain in a Sylgard™ compression sample. The eight lines correspond to 8 images representing the global strain in the y-direction from 0-12.59%. There is a slight deviation from symmetry as strain increases, this is one of the reasons why the modulus of the material is only calculated using the strain from 0-10%.

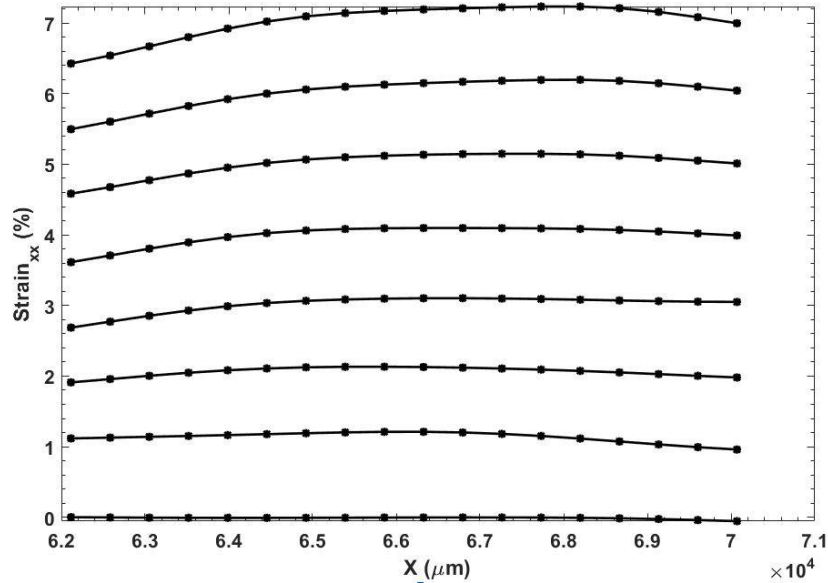


Figure 58. Strain in x-direction along the horizontal line half-way from top of ROI.

The strain pattern depicted in Figure 58 shows the strain in the x-direction. It is observed that as the strain increases the line scan takes a curved shape. This means that the center of the sample is stretching outward at a higher rate compared to the parts near the end of the sample. This is to be expected of rubbery materials as the materials in the center has much more room to move compared to the material on the edges.

4.6 Mechanical Property Characterization of PDMS in Tension

This section will discuss mechanical properties of the Sylgard and Gelest samples that were tested in tension and compression. The tension samples were tested until failure and their strain measured using the video extensimeter. The compression samples were also tested up to failure and the strain tracked using the crosshead displacement. The failure strains were obtained from this. The modulus from all the samples were obtained by calculating the slope of the stress-strain curve using the data from DIC from 0% to 20%.

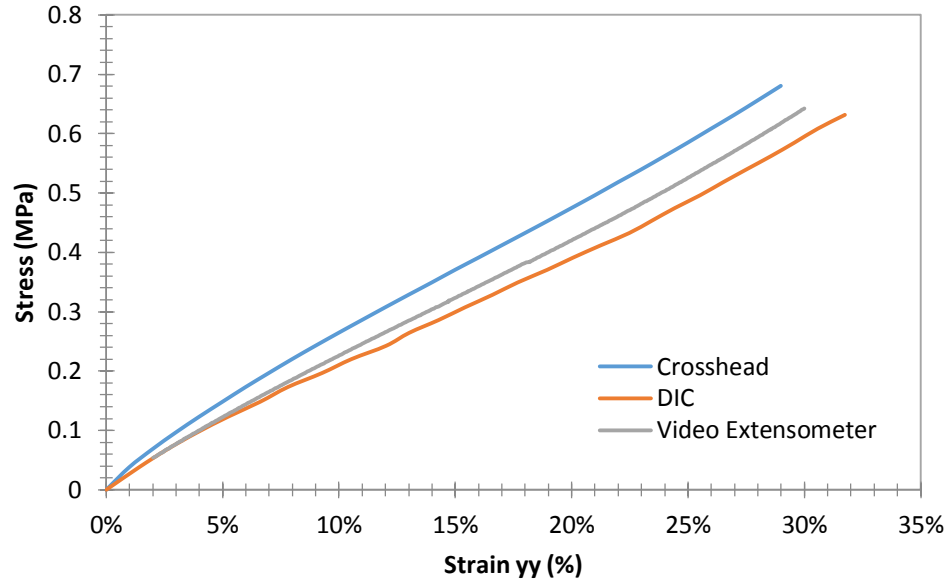


Figure 59. Comparison of different strain measurement techniques.

Figure 59 illustrates a clear comparison between the three different strain techniques that were employed in the calculation of material characteristics and properties. Young's modulus from crosshead reading was 2.21MPa, 2.03MPa from video extensometer and 1.89MPa from DIC. Young's modulus was calculated from 2% to 20% strain. The strain values from DIC closely matched the ones from the video extensometer. While the video extensometer takes readings from two points, DIC takes readings from the entire region of interest on the gage section thereby tracking multiple points. The DIC data was only recorded up to 30% strain because higher strain values are distorted by accumulated error from correlating numerous images.

Figure 60 shows the strain plots for the Sylgard samples while Figure 61 shows the strain plots for the Gelest tension samples.

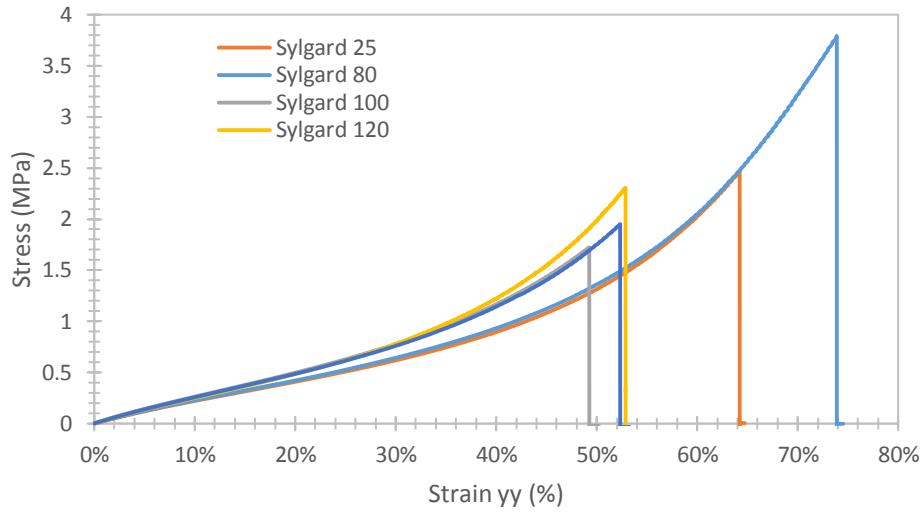


Figure 60. Stress-strain relationship of Sylgard samples in tension up to failure.

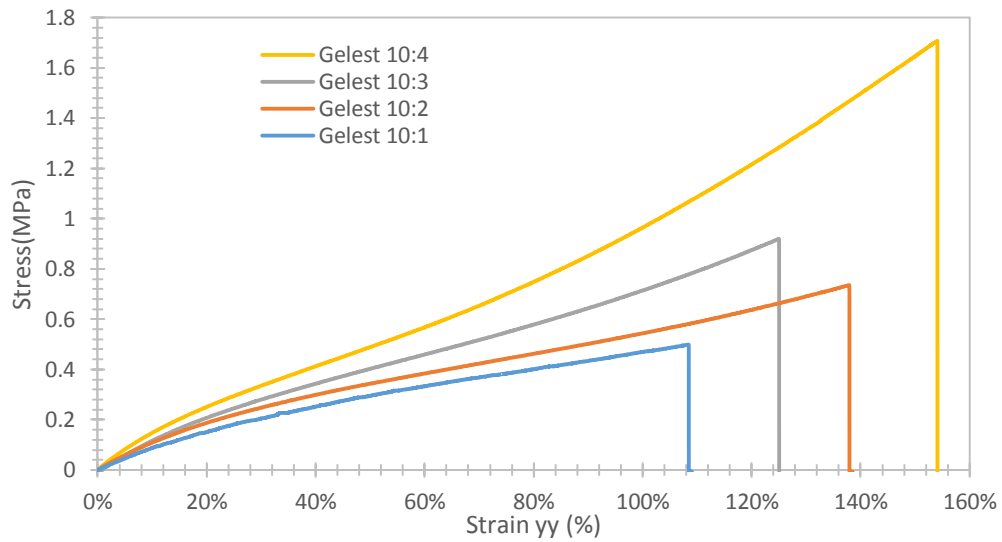


Figure 61. Stress-strain relationship of Gelest samples in tension up to failure

The results of tension and compression PDMS samples with various silica content and cured at different temperatures are presented in Table 5 and Table 6 below. The results in Table 4 are from the video extensometer device since it could accurately capture the strain field on the sample up to failure. Table 5 results were from the

crosshead since in compression the video extensometer cannot ‘see’ the marks made on the sample as it compressed up to a thickness of one millimeter.

Table 5: Mechanical properties and characteristics of PDMS in tension.

Sample	Cure Temperature (°C)	Silica Content %	Failure Strain (mm/mm)	Failure Strength (MPa)	Modulus (MPa)	Poisson Ratio
Sylgard 25	25	~40	0.65	2.29	1.868	0.462
Sylgard 80	80	~40	0.7	3.2	1.9555	0.468
Sylgard 100	100	~40	0.52	1.95	2.3015	0.458
Sylgard 120	120	~40	0.55	2.285	2.3545	0.415
Sylgard 150	150	~40	0.52	1.91	2.335	0.365
Gelest 10:1	80	9	1.005	0.47	0.707	0.404
Gelest 10:2	80	16	1.395	1.065	0.866	0.424
Gelest 10:3	80	22	1.35	1.165	1.0415	0.441
Gelest 10:4	80	30	1.525	1.69	1.138	0.421

For the tension samples there was a noticeable difference in the failure strain between the Sylgard and Gelest samples. The Sylgard samples showed a decreasing failure strain with increasing cure temperature. This indicates that there is a significant material change at higher cure temperatures. While the modulus increased, the material became stiffer, it also failed earlier. 80°C seems to be the temperature at which the Sylgard samples transitioned in mechanical characteristics. Gelest samples in tension had a higher failure strain compared to the Sylgard samples. The modulus and failure strength was significantly lower compared to the Sylgard cured at the same temperature. Decreasing the silica content only improved the flexibility of the material evident by the increased failure strain.



Figure 62. Typical failure PDMS sample under tension.

Figure 62 shows a failed tension sample that was tested using a video extensometer. The sample snapped in the middle proving that the gage section was experiencing the most amount of stress and strain. The two dots are the points which were being tracked by the video extensometer.

4.7 Mechanical Property Characterization of PDMS in Compression

Figure 63 and Figure 64 below show the compression failure plots for Sylgard and Gelest respectively. The tension samples were tested at 10% strain per minute, around 6.5mm per minute and the samples were tested until failure.

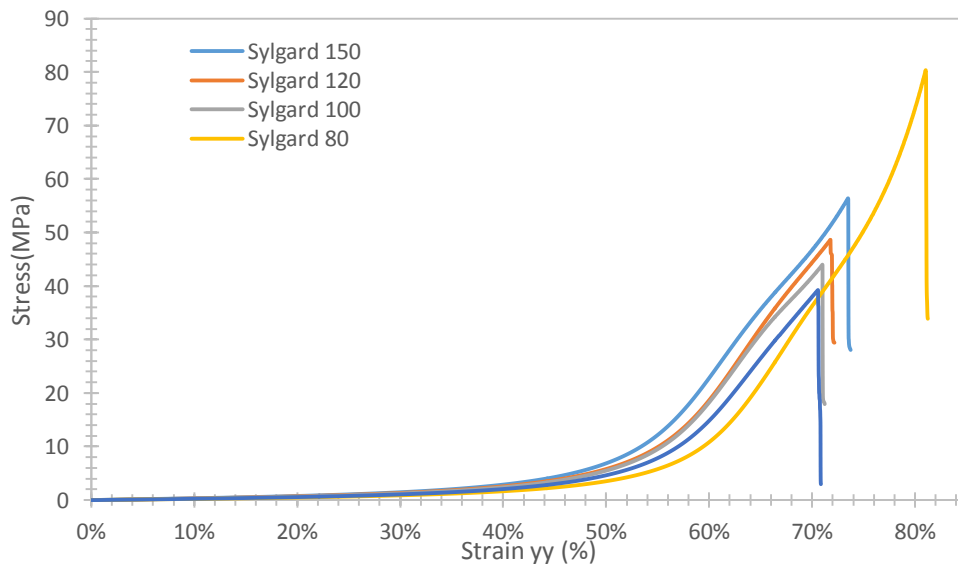


Figure 63. Stress-strain relationship of Sylgard samples in compression up to failure.

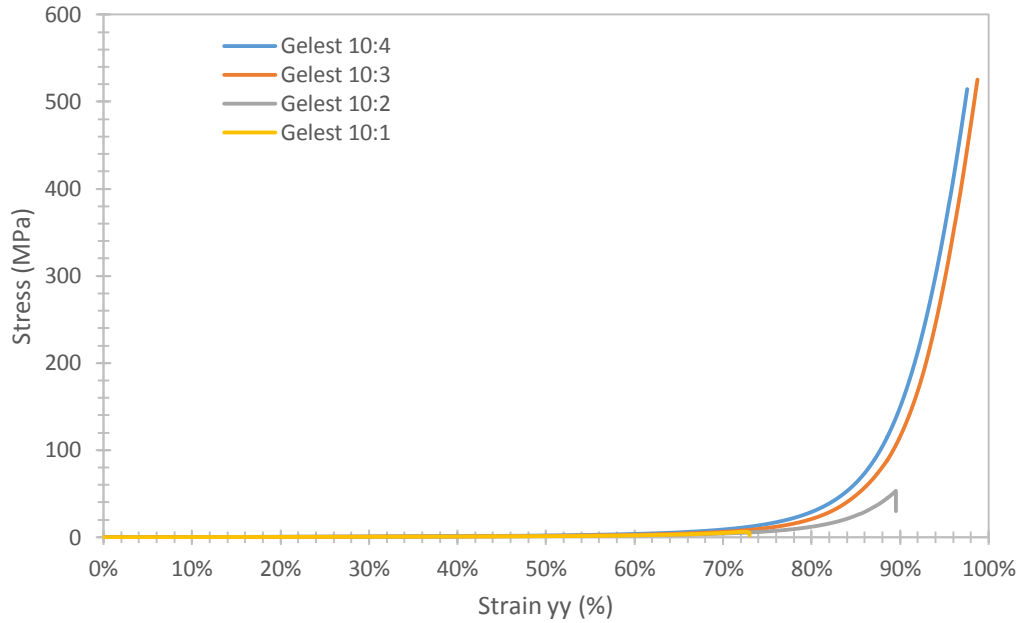


Figure 64. Stress-strain relationship of Gelest samples in tension up to failure.

The results from Figure 63 and Figure 64 are documented in Table 6 below. The failure strain was higher in the Gelest samples. Since they were more flexible, they failed at higher strength values. This is because they contained less silica compared to the Sylgard samples. Consequently, their modulus was lower for the same reason. It was interesting to note that the failure strength was significantly higher in the Gelest samples. The last two samples, Gelest 10:3 and Gelest 10:4 reached the limit of the Instron testing machine, 50,000lb. The samples only failed the instant the machine retracted because the load cell limit was reached.

Table 6: Mechanical properties and characterization of PDMS in compression.

Sample	Cure Temperature (°C)	Silica Content %	Failure Strain (mm/mm)	Failure Strength (MPa)	Modulus (MPa)	Poisson Ratio
Sylgard 25	25	~40	0.71	43.62	2.52	0.600
Sylgard 80	80	~40	0.83	86	2.25	0.585
Sylgard 100	100	~40	0.71	44	2.99	0.570

Sylgard 120	120	~40	0.71	48.63	3.33	0.545
Sylgard 150	150	~40	0.73	56.38	3.65	0.700
Gelest 10:1	80	9	0.72	6.25	1.49	0.405
Gelest 10:2	80	16	0.90	51	1.62	0.490
Gelest 10:3	80	22	0.95	310	1.92	0.546
Gelest 10:4	80	30	0.97	522	2.29	0.602



Figure 65. Typical failure PDMS sample under compression.

Figure 65 shows a shattered compression sample after the load was released instantaneously. The sample exhibited glass like behavior upon failure. The steepness of the stress-strain plot at strain values above 0.8 mm/mm support this behavior.

4.8 Effect of cure temperature on Sylgard® 184

From Figure 66 the modulus in both the tension and compression samples increased with the cure temperature. There is a 25% increase in the young's modulus of the tension sample and a 32% increase in the modulus of the compression sample when the cure temperature was changed from 25°C to 150°C. At higher cure temperatures, thermosetting PDMS resin hardens more and achieves a higher modulus.

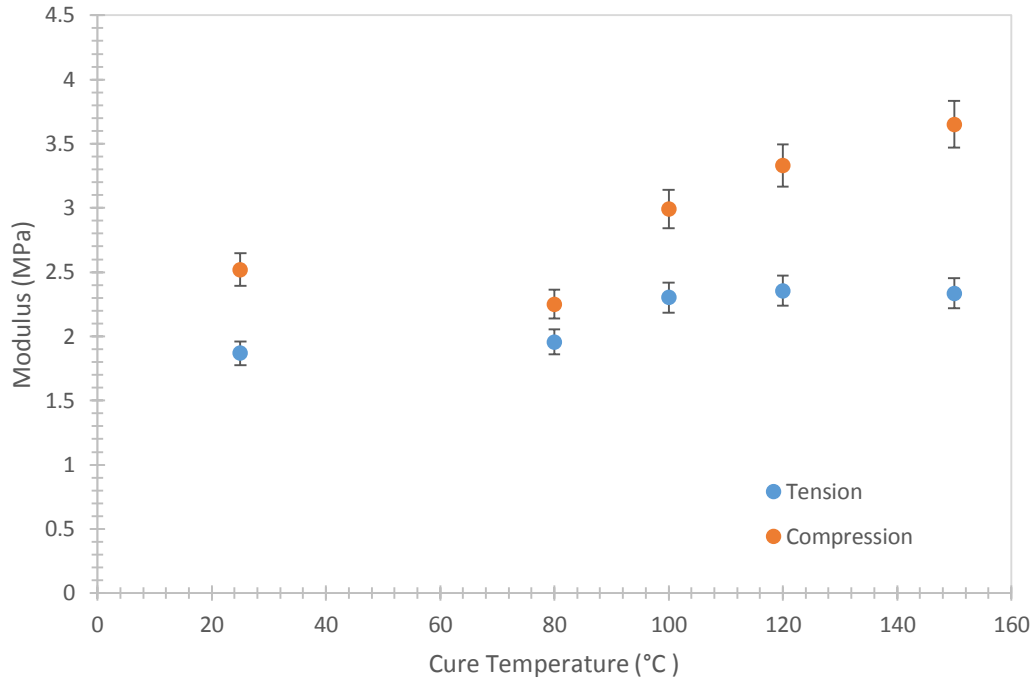


Figure 66. Cure temperature effect on Young's modulus.

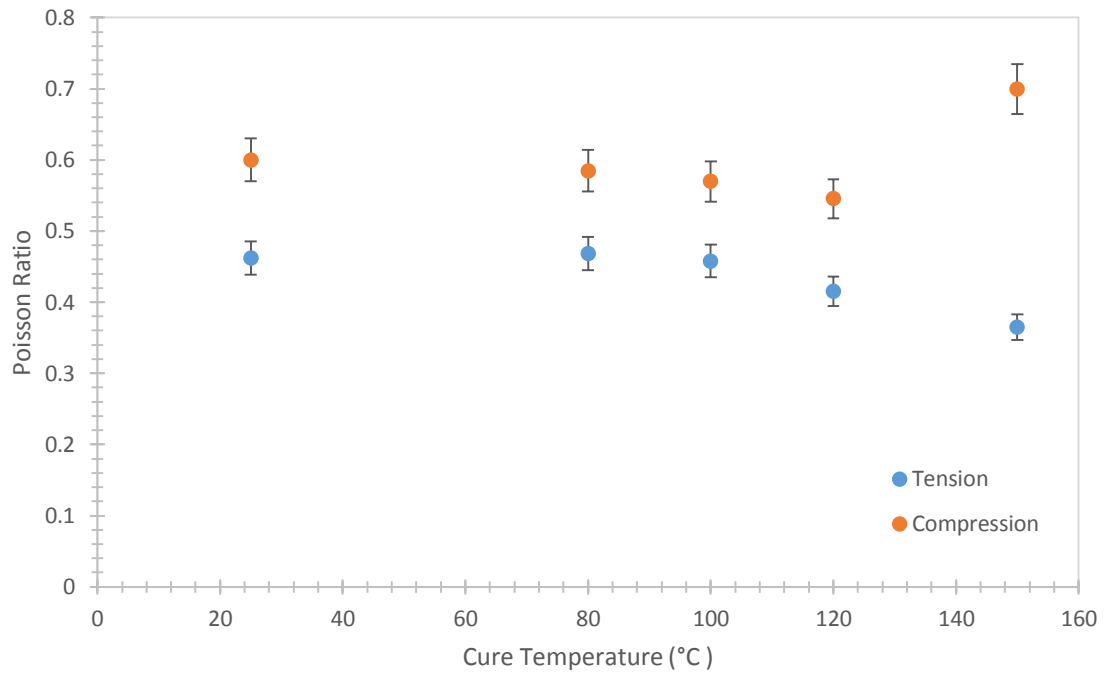


Figure 67. Poisson ratio change with cure temperature.

From Figure 67 above the Poisson ratio decreased by 21% from 0.426 for the sample cured at 25°C to 0.365 for the sample cured at 150°C in tension. The increase in modulus with increased cure temperature made the sample more rigid therefore the change in the y-direction is slower for the sample cured at higher temperatures. Similarly, in the compression sample, an increase in the modulus at higher temperatures led to sample that is more resistant to deformation in the y-direction resulting to an increase in the Poisson ratio.

4.9 Effect of silica content on Gelest

The modulus of the tension sample increased by 61% with a 21% increase in silica, a 3:1 ratio. This proves that the silica in the Gelest™ material is responsible for most of the mechanical properties. The modulus in the compression sample increased by 54% with a 21% increase in silica, a 2.6:1 ratio. The increase is significant to conclude that the silica in the compression samples was also responsible for most of the mechanical characteristics.

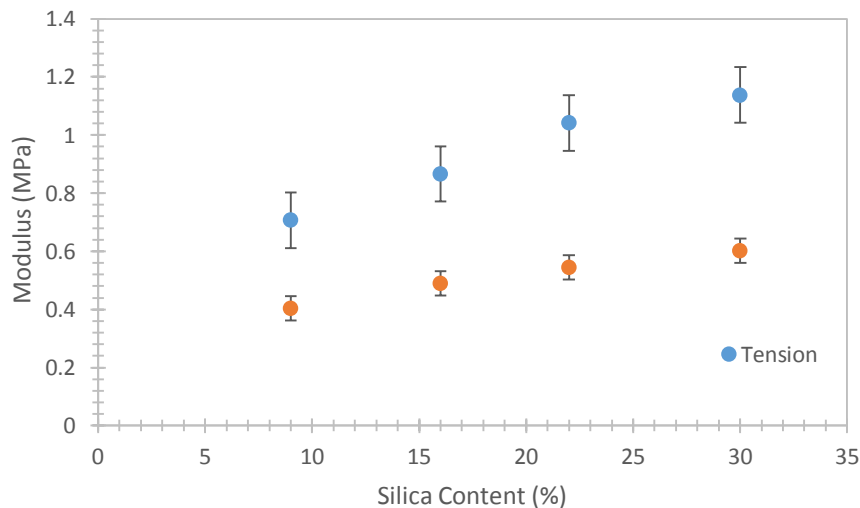


Figure 68. Effect of silica on compression modulus of Gelest samples.

Figure 69 below shows an increase in the Poisson ratio for the compression samples from 0.4045 to 0.6016 as the silica content in the sample was increased from 9% to 30%. As silica is increased, the material is more resistant to deformation and hence the deformation in the y-direction is lower with an increase in silica for the same amount of load. Similarly, the increase in silica from 9% to 30% led to an increase in the Poisson ratio from 0.407 to 0.421 for the tension samples. This means that the increase in silica made the samples more rigid hence relatively resistant to deformation in the y-direction.

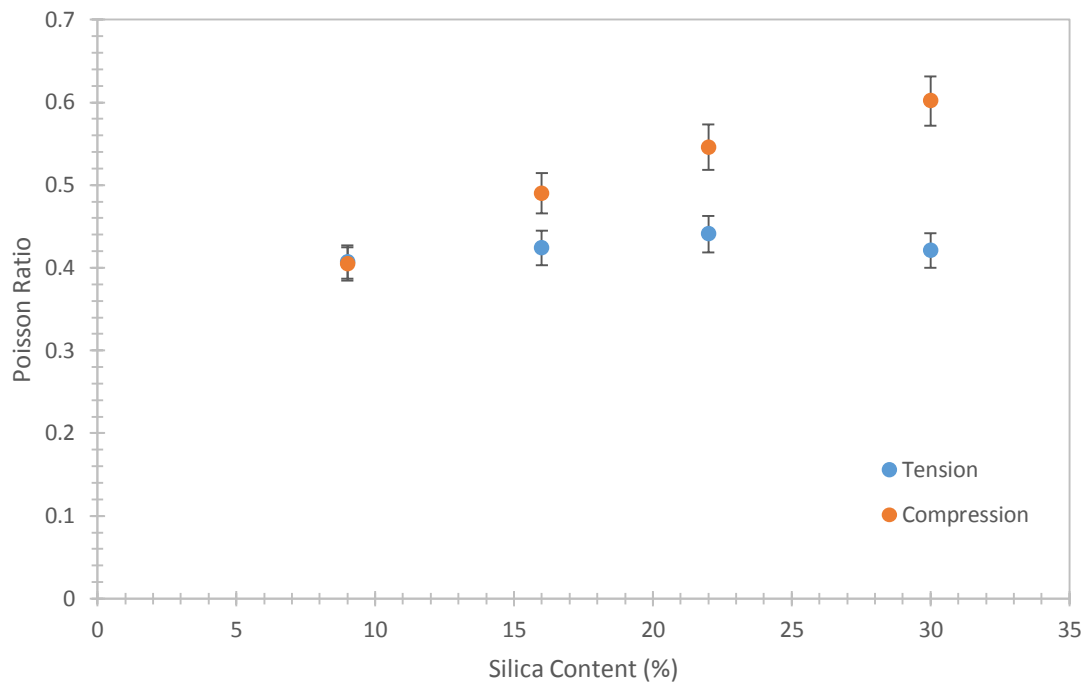


Figure 69. Effect of silica on Poisson ratio of Gelest samples.

CHAPTER 5: SUMMARY AND FUTURE WORK

The gage section of a PDMS sample cut out according to ASTM D412-C standard experiences 20% more strain than the crosshead. A non-contact method is recommended for testing strain of hyper-elastic materials since the strain is non-linear after 20%. Dynamic Mechanical Analysis reveals that the glass transition temperature is unchanged by the temperature at which the sample was cured. Thermogravimetric analysis conformed that a 1% increase in residual mass after 800°C requires ~9.32% increase in silica content in the Gelest™ samples.

The Finite Element Analysis proved that the strain in the gage section of a dogbone sample is uniform and undisturbed. This highlights the importance of measuring strain from the gage section as opposed to taking it from the crosshead. The digital image correlation from the Matlab code proved that the Poisson ratio for PDMS in tension is 0.4147 and 0.6076 in compression. This means that in tension the sample is extending in the y-direction at a higher rate than in the x-direction relatively compared to the sample in compression which stretches at a higher rate in the x-direction than in the y-direction.

DIC is a better method for tension and compression testing of hyper-elastic materials. In addition to accurate stress-strain plots, we can also calculate the Poisson ratio of materials at different strains. Researchers should utilize this technique in the development of polymers in order to accurately characterize the mechanical properties. Accurate stress-strain plots and the Poisson ratio can be used in finite element analysis to predict material behavior under different conditions.

Equipment setup is critical in achieving accurate results from the DIC, the calculations assume that the sample is planar, parallel to and at a constant distance from the visual sensor during the entire experiment. Failure to ensure this will lead to

significant shear strain which alter the accuracy of the test. Also, sufficient illumination is a critical factor for obtaining high quality images, the analysis will benefit from the light to a large extent, and the light direction should also be vertical to the sample surface, otherwise shades result from irregularity of the surface will change and therefore affect the correctness of analysis.

REFERENCES

- [1] Ashruf, C. M. A. (2002). Thin flexible pressure sensors. *Sensor Review*, 22(4), 322-327.
- [2] Segev-Bar, M., & Haick, H. (2013). Flexible sensors based on nanoparticles. *American Chemical Society*, 7 (10), 8366–8378.
- [3] Simscale. Hyperelastic Materials. Retrieved from <https://www.simscale.com/docs/content/simulation/model/materials/hyperelasticMaterial.html>.
- [4] Kim, T. K., Kim, J. K., & Jeong, O. C. (2011). Measurement of nonlinear mechanical properties of PDMS elastomer. *Microelectronic Engineering*, 88(8), 1982-1985.
- [5] Wang, Z. (2011). *Polydimethylsiloxane mechanical properties measured by macroscopic compression and nanoindentation techniques* (Doctoral dissertation).
- [6] Zhou, J., Khodakov, D. A., Ellis, A. V., & Voelcker, N. H. (2012). Surface modification for PDMS-based microfluidic devices. *Electrophoresis*, 33(1), 89-104.
- [7] Jung, E. S., Oh, T. H., & Kwon, S. Micro PDMS hydrogen generator using hydrolysis of sodium borohydride over cobalt nickel-foam catalyst and immobilized cobalt-PH₃PO/PDMS. *SIO₂ catalyst*.
- [8] Kim, T. K., Kim, J. K., & Jeong, O. C. (2011). Measurement of nonlinear mechanical properties of PDMS elastomer. *Microelectronic Engineering*, 88(8), 1982-1985.
- [9] Tsvetkov, S., Gateva, S., Taslakov, M., Mariotti, E., & Cartaleva, S. (2014). Light-induced atomic desorption in cells with different PDMS coatings. *Journal of Physics: Conference Series* (Vol. 514, No. 1, p. 012030). IOP Publishing.
- [10] Dollase, T., Wilhelm, M., Spiess, H. W., Yagen, Y., Yerushalmi-Rozen, R., & Gottlieb, M. (2003). Effect of interfaces on the crystallization behavior of PDMS. *Interface Science*, 11(2), 199-209.
- [11] Kuo, A. C. (1999). Poly (dimethylsiloxane). *Polymer Data Handbook*, 411-435.
- [12] Owen, M. J. (1981). Why silicones behave funny. *Chemtech*, 11(5), 288-292.
- [13] Vaid, A., Singh, R., & Lehana, P. (2013). Development of microchannel fabrication technique and method to increase trench depth on PDMS. *International Journal of Advanced Research in Computer and Communication Engineering*, 2(12), 2278-1021.
- [14] Lawrenson, A., Barnes, K., & Greeves, N. (2008). ChemTube3D interactive 3D organic reaction mechanisms. *ChemTube3D*.

- [15] Schneider, F., Fellner, T., Wilde, J., & Wallrabe, U. (2008). Mechanical properties of silicones for MEMS. *Journal of Micromechanics and Microengineering*, 18(6), 065008
- [16] Peters, W. H., & Ranson, W. F. (1982). Digital imaging techniques in experimental stress analysis. *Optical Engineering*, 21(3), 213427-213427.
- [17] Tong, W. (2013). Formulation of Lucas–Kanade digital image correlation algorithms for non-contact deformation measurements: a review. *Strain*, 49(4), 313-334.
- [18] Pritchard, R. H., Lava, P., Debruyne, D., & Terentjev, E. M. (2013). Precise determination of the Poisson ratio in soft materials with 2D digital image correlation. *Soft Matter*, 9(26), 6037-6045.
- [19] Post, D. (1983). Moiré interferometry at VPI & SU. *Experimental Mechanics*, 23(2), 203-210.
- [20] Gottenberg, W. G. (1968). Some applications of holographic interferometry. *Experimental Mechanics*, 8(9), 405-410.
- [21] Wang, Y. Y., Chen, D. J., & Chiang, F. P. (1993). Material testing by computer aided speckle interferometry. *Experimental Techniques*, 17(5), 30-32.
- [22] Bastawros, A. F., & Voloshin, A. S. Thermal strain measurements in electronic packages through fractional fringe moiré interferometry. *Journal of Electronic Packaging*, 1990, 112(4), 303-308.
- [23] Bruck, H. A., McNeill, S. R., Sutton, M. A., & Peters, W. H. (1989). Digital image correlation using Newton-Raphson method of partial differential correction. *Experimental Mechanics*, 29(3), 261-267.
- [24] Sutton, M. A., Wolters, W. J., Peters, W. H., Ranson, W. F., & McNeill, S. R. (1983). Determination of displacements using an improved digital correlation method. *Image and Vision Computing*, 1(3), 133-139.
- [25] Sutton, M. A., Mingqi, C., Peters, W. H., Chao, Y. J., & McNeill, S. R. (1986). Application of an optimized digital correlation method to planar deformation analysis. *Image and Vision Computing*, 4(3), 143-150.
- [26] Sutton, M. A., Mingqi, C., Peters, W. H., Chao, Y. J., & McNeill, S. R. (1986). Application of an optimized digital correlation method to planar deformation analysis. *Image and Vision Computing*, 4(3), 151-155.
- [27] Zhang, D., Zhang, X., & Cheng, G. (1999). Compression strain measurement by digital speckle correlation. *Experimental Mechanics*, 39(1), 62-65.

- [28] Lu, H., Yeh, C. P., & Wyatt, K. (1998). Experimental evaluation of solder joint thermal strain in a CSP using digital speckle correlation. *Thermal and Thermomechanical Phenomena in Electronic Systems, 1998. ITherm'98. The Sixth Intersociety Conference*, 4(8), 241-245.
- [29] McCormick, N., & Lord, J. D. (2012). Digital Image Correlation. *Materials Today*.13(12), 52-54.
- [30] Fan, X. (2004). *Study on the speckle image correlation* (Doctoral dissertation).
- [31] Mathworks. (2012). Normalized 2-D cross-correlation (normxcorr2). Retrieved from <https://www.mathworks.com/help/images/ref/normxcorr2.html>
- [32] Dow Corning. (2000). Sylgard 184 Silicone Elastomer Kit. Retrieved from <http://www.dowcorning.com/applications/search/products/Details.aspx?prod=01064291>
- [33] Andy, H. (2013). Gas pycnometer equation. Retrieved from <http://pycnometer-analyzer.blogspot.com/2013/09/gas-pycnometer-equation.html>.
- [34] Micromeritics.(1999).AccuPyc II 1340 Pycnometer. Retrieved from <http://www.micromeritics.com/Product-Showcase/AccuPyc-II-1340.aspx>
- [35] Foreman, J. (1997). Dynamic mechanical analysis of polymers. *American Laboratory*, 29, 21-24.
- [36] Kwan Jr, K. S. (1998). *The role of penetrant structure on the transport and mechanical properties of a thermoset adhesive* (Doctoral dissertation).
- [37] Turi, E. (Ed.). (2012). *Thermal characterization of polymeric materials*. Elsevier. 980-982.
- [38] TA Instruments. *Measurement of the glass transition temperature using dynamic mechanical analysis*. Retrieved from <http://www.tainstruments.com/pdf/literature/TS64.pdf>.
- [39] Canon. EOS Rebel T5i Body. Retrieved from <https://shop.usa.canon.com/shop/en/catalog/>
- [40] Joshi, V. S., Lee, G. F., & Santiago, J. R. (2017, January). Dynamic characterization and modeling of potting materials for electronics assemblies. *AIP Conference Proceedings*, 1793(1), 110013.
- [41] Crowe-Willoughby, J. A., Weiger, K. L., Özçam, A. E., & Genzer, J. (2010). Formation of silicone elastomer networks films with gradients in modulus. *Polymer*, 51(3), 763-773.

- [42] Hu, L., Hecht, D. S., & Grüner, G. (2004). Percolation in transparent and conducting carbon nanotube networks. *Nano letters*, 4(12), 2513-2517.
- [43] Sandler, J. K. W., Kirk, J. E., Kinloch, I. A., Shaffer, M. S. P., & Windle, A. H. (2003). Ultra-low electrical percolation threshold in carbon-nanotube-epoxy composites. *Polymer*, 44(19), 5893-5899.
- [44] Choi, K. M., & Rogers, J. A. (2003). A photocurable poly (dimethylsiloxane) chemistry designed for soft lithographic molding and printing in the nanometer regime. *Journal of the American Chemical Society*, 125(14), 4060-4061.
- [45] Studer, V., Hang, G., Pandolfi, A., Ortiz, M., French Anderson, W., & Quake, S. R. (2004). Scaling properties of a low-actuation pressure microfluidic valve. *Journal of Applied Physics*, 95(1), 393-398.

APPENDIX

Correlation algorithm : cporr_mod.m

```
function [xyinput,corr_coeff] = cpcorr_mod(varargin)
%CPCORR Tune control point locations using cross-correlation.
% INPUT_POINTS = CPCORR(INPUT_POINTS_IN,BASE_POINTS_IN,INPUT,BASE)
uses
% normalized cross-correlation to adjust each pair of control points
% specified in INPUT_POINTS_IN and BASE_POINTS_IN.
%
% INPUT_POINTS_IN must be an M-by-2 double matrix containing the
% coordinates of control points in the input image. BASE_POINTS_IN
is
% an M-by-2 double matrix containing the coordinates of control
points
% in the base image.
%
% CPCORR returns the adjusted control points in INPUT_POINTS, a
double
% matrix the same size as INPUT_POINTS_IN. If CPCORR cannot
correlate a
% pairs of control points, INPUT_POINTS will contain the same
coordinates
% as INPUT_POINTS_IN for that pair.
%
% CPCORR will only move the position of a control point by up to 4
% pixels. Adjusted coordinates are accurate up to one tenth of a
% pixel. CPCORR is designed to get subpixel accuracy from the image
% content and coarse control point selection.
% NOTE: EJ modification: CPCORR_MOD will adjust the control point
by
% more than 4 pixels, depending on the subset size!!
%
% Note that the INPUT and BASE images must have the same scale for
% CPCORR to be effective.
%
% CPCORR cannot adjust a point if any of the following occur:
% - points are too near the edge of either image
% - regions of images around points contain Inf or NaN
% - region around a point in input image has zero standard
deviation
% - regions of images around points are poorly correlated
%
% Class Support
% -----
% The images can be numeric and must contain finite values. The input
% control point pairs are double.
%
% Example
% -----
% This example uses CPCORR to fine-tune control points selected in an
% image. Note the difference in the values of the INPUT_POINTS
matrix
% and the INPUT_POINTS_ADJ matrix.
%
% input = imread('onion.png');
```

```

%     base = imread('peppers.png');
%     input_points = [127 93; 74 59];
%     base_points = [323 195; 269 161];
%     input_points_adj = cpcorr(input_points,base_points,...
%                               input(:,:,1),base(:,:,1))
%
% See also CP2TFORM, CPSELECT, NORMXCORR2, IMTRANSFORM.

% Copyright 1993-2011 The MathWorks, Inc.
% $Revision: 1.16.4.10 $ $Date: 2011/08/09 17:49:27 $

% Input-output specs
% -----
% INPUT_POINTS_IN: M-by-2 double matrix
%                 INPUT_POINTS_IN(:)>=0.5
%                 INPUT_POINTS_IN(:,1)<=size(INPUT,2)+0.5
%                 INPUT_POINTS_IN(:,2)<=size(INPUT,1)+0.5
%
% BASE_POINTS_IN: M-by-2 double matrix
%                 BASE_POINTS_IN(:)>=0.5
%                 BASE_POINTS_IN(:,1)<=size(BASE,2)+0.5
%                 BASE_POINTS_IN(:,2)<=size(BASE,1)+0.5
%
% INPUT:  2-D, real, full matrix
%         logical, uint8, uint16, or double
%         must be finite (no NaNs, no Infs inside regions being
correlated)
%
% BASE:   2-D, real, full matrix
%         logical, uint8, uint16, or double
%         must be finite (no NaNs, no Infs inside regions being
correlated)

[xyinput_in,xybase_in,input,base,subset,search_zone,thresh] =
ParseInputs(varargin{:});

CORRSIZE = subset/2;
ncp = size(xyinput_in,1);

% get all rectangle coordinates
rects_input = calc_rects(xyinput_in,ones(ncp,1)*CORRSIZE,input);
rects_base = calc_rects(xybase_in,search_zone*CORRSIZE,base);

xyinput = xyinput_in; % initialize adjusted control points matrix
corr_coeff = zeros(size(xyinput,1),1);

for icp = 1:ncp

    %Check to see if the current point is a NaN pt
    if isnan(xybase_in(icp,1)) || isnan(xyinput_in(icp,1))
        xyinput(icp,:) = NaN;
        continue
    end
end

```

```

if isequal(rects_input(icp,3:4),[0 0]) || ...
    isequal(rects_base(icp,3:4),[0 0])
    % near edge, unable to adjust
    xyinput(icp,:) = NaN;
    continue
end

%EJ: New check: Moved this check from the ParseInputs function
if xyinput_in(icp,1)<0.5 || xyinput_in(icp,2)<0.5 || ...
    xyinput_in(icp,1)>size(input,2)+0.5 ||
xyinput_in(icp,2)>size(input,1)+0.5
    %Control point is outside of the image
    xyinput(icp,:) = NaN;
    continue
end

if xybase_in(icp,1)<0.5 || xybase_in(icp,2)<0.5 || ...
    xybase_in(icp,1)>size(input,2)+0.5 ||
xybase_in(icp,2)>size(input,1)+0.5
    %Control point is outside of the image
    xyinput(icp,:) = NaN;
    continue
end

sub_input = imcrop(input,rects_input(icp,:));
sub_base = imcrop(base,rects_base(icp,:));

inputsize = size(sub_input);

% make sure finite
if any(~isfinite(sub_input(:))) || any(~isfinite(sub_base(:)))
    % NaN or Inf, unable to adjust
    xyinput(icp,:) = NaN;
    continue
end

% check that template rectangle sub_input has nonzero std
if std(sub_input(:))==0
    % zero standard deviation of template image, unable to adjust
    xyinput(icp,:) = NaN;
    continue
end

norm_cross_corr = normxcorr2(sub_input,sub_base);

% get subpixel resolution from cross correlation
subpixel = true;
[xpeak, ypeak, amplitude] = findpeak(norm_cross_corr,subpixel);

%save the correlation coefficient:
corr_coeff(icp) = amplitude; %EJ modification 140610

% eliminate any poor correlations
% THRESHOLD = 0.5; %original
THRESHOLD = thresh; %EJ modification 140610

```

```

if (amplitude < THRESHOLD)
    % low correlation, unable to adjust
    xyinput(icp,:) = NaN;
    continue
end

% offset found by cross correlation
%   corr_offset = [ (xpeak-inputsize(2)-CORRSIZE)
%   (ypeak-inputsize(1)-CORRSIZE) ]; %Original code
zero_disp = ceil(size(norm_cross_corr)/2); %location in the
normcrosscorr that corresponds to zero displacement
corr_offset = [xpeak,ypeak] - zero_disp;

% eliminate any big changes in control points
%   ind = find(abs(corr_offset) > (CORRSIZE-1), 1); %Original code
max_disp = search_zone(icp)*CORRSIZE - CORRSIZE - 1; %EJ: use when
undeformed subset size is different from 2X deformed subset size
ind = find(abs(corr_offset) > max_disp, 1);
if ~isempty(ind)
    % peak of norxcorr2 not well constrained, unable to adjust
    xyinput(icp,:) = NaN;
    corr_coeff(icp) = -1;
    continue
end

input_fractional_offset = xyinput(icp,:) -
round(xyinput(icp,:)*1000)/1000;
base_fractional_offset = xybase_in(icp,:) -
round(xybase_in(icp,:)*1000)/1000;

% adjust control point
xyinput(icp,:) = xyinput(icp,:) - input_fractional_offset -
corr_offset + base_fractional_offset;

end

%-----
%
function rect = calc_rects(xy,halfwidth,img)

% Calculate rectangles so imcrop will return image with xy coordinate
inside center pixel

default_width = 2*halfwidth;
default_height = default_width;

% xy specifies center of rectangle, need upper left
% upperleft = round(xy) - halfwidth; %Original line of code
upperleft = round(xy) - [halfwidth,halfwidth]; %EJ modification

```

```

% need to modify for pixels near edge of images
upper = upperleft(:,2);
left = upperleft(:,1);
lower = upper + default_height;
right = left + default_width;
% width = default_width * ones(size(upper)); %Original line of code
% height = default_height * ones(size(upper)); %Original line of code
width = default_width; %EJ modification
height = default_height; %EJ modification

% check edges for coordinates outside image
[upper,height] = adjust_lo_edge(upper,1,height);
[~,height] = adjust_hi_edge(lower,size(img,1),height);
[left,width] = adjust_lo_edge(left,1,width);
[~,width] = adjust_hi_edge(right,size(img,2),width);

% set width and height to zero when less than default size
iw = find(width<default_width);
ih = find(height<default_height);
idx = unique([iw; ih]);
width(idx) = 0;
height(idx) = 0;

rect = [left upper width height];

%-----
%
function [coordinates, breadth] =
adjust_lo_edge(coordinates,edge,breadth)

indx = find( coordinates<edge );
if ~isempty(indx)
    breadth(indx) = breadth(indx) - abs(coordinates(indx)-edge);
    coordinates(indx) = edge;
end

%-----
%
function [coordinates, breadth] =
adjust_hi_edge(coordinates,edge,breadth)

indx = find( coordinates>edge );
if ~isempty(indx)
    breadth(indx) = breadth(indx) - abs(coordinates(indx)-edge);
    coordinates(indx) = edge;
end

%-----
%
function [xyinput_in,xybase_in,input,base,subset,search_zone,thresh] =
ParseInputs(varargin)

% narginchk(4,5);

xyinput_in = varargin{1};

```

```

xybase_in = varargin{2};
if size(xyinput_in,2) ~= 2 || size(xybase_in,2) ~= 2
    error(message('images:cpcorr:cpMatrixMustBeMby2'))
end

if size(xyinput_in,1) ~= size(xybase_in,1)
    error(message('images:cpcorr:needSameNumOfControlPoints'))
end

input = varargin{3};
base = varargin{4};
if ndims(input) ~= 2 || ndims(base) ~= 2
    error(message('images:cpcorr:intensityImagesReq'))
end

input = double(input);
base = double(base);

%Original Check:
% if any(xyinput_in(:)<0.5) || any(xyinput_in(:,1)>size(input,2)+0.5)
% || ...
%     any(xyinput_in(:,2)>size(input,1)+0.5) || ...
%     any(xybase_in(:)<0.5) || any(xybase_in(:,1)>size(base,2)+0.5) ||
%     ...
%     any(xybase_in(:,2)>size(base,1)+0.5)
%     error(message('images:cpcorr:cpPointsMustBeInPixCoord'))
% end

%EJ New Check:
%Eliminate the check on the base and input points; instead, move this
check to
%within the loop over the control points.  If a base or input point is
out of the
%image, make that point not correlate.  (Note that originally, I only
moved
%the check on the input points into the loop; this works if you are
using
%image 1 as the reference image, and so the xybase_in are the grid
points.
%But if you use the preceding image as the reference image, then the
%xybase_in points are the valid_points from the previous correlation,
and
%so they have the possibility to be out of the image

subset = varargin{5};
search_zone = varargin{6};
thresh = varargin{7};

```